Role of secondary phases and thermal cycling on thermoelectric properties of TiNiSn half-Heusler alloy prepared by different processing routes

Role of secondary phases and thermal cycling on thermoelectric properties of TiNiSn half-Heusler alloy prepared by different processing routes

Francesco Aversano[1], Mauro Palumbo[1,*], Alberto Ferrario[2], Stefano Boldrini[2], Carlo Fanciulli[3], Marcello Baricco[1], Alberto Castellero[1]

[1]University of Turin, Department of Chemistry & NIS, Turin, Italy

[2]CNR – ICMATE, Padova Unit, Padova, Italy

[3]CNR – ICMATE, Lecco Unit, Lecco, Italy

*Corresponding author: Mauro Palumbo; Tel. +39 0116707913; Fax: +39 0116707855; e-mail: mauro.palumbo@unito.it

Abstract

Samples of a TiNiSn half-Heusler thermoelectric alloy were prepared using arc melting and rapid solidification by planar flow casting. On the one hand, arc melted samples show multiple phases and need long annealing time to be homogenized into a single phase. On the other hand, rapidly solidified samples show an almost single phase, with a grain refined microstructure. This result is a consequence of the melt undercooling, that allows to bypass the primary solidification of TiNi2Sn full-Heusler and to hinder grain growth. Rapidly solidified samples were consolidated into dense bulk samples by means of open die pressing. The grain refined microstructure obtained by rapid solidification is maintained after sintering, leading to a reduced lattice thermal conductivity, due to a scattering of phonons at grain boundaries. The role of the residual secondary phases (Ni3Sn4, TiNi2Sn and Sn) on the electrical conductivity and thermopower

is discussed in the framework of the effective medium theory and related models, explaining the dispersion of thermoelectric properties observed in the literature for nominally stoichiometric TiNiSn. Thermal cycling above 700 K causes surface oxidation, leading to altered thermoelectric properties.

Keywords: Rapid solidification, half-Heusler, secondary phases, thermoelectric properties, effective medium theory.

1. Introduction

The thermoelectric effect allows to convert temperature gradients directly into an electrical current and can be used for energy harvesting from waste heat source in industrial, domestic and transport environments [1, 2]. Despite current thermoelectric materials are limited in conversion efficiency, thermoelectricity has attracted great interest in the last years, due to the compactness, reliability and durability of the devices, together with the absence of fluid and moving parts [3]. The performance of thermoelectric materials can be evaluated by the dimensionless figure of merit $ZT = \frac{\alpha^2\sigma}{\kappa_{lat}+\kappa_{el}}T$, where α is the Seebeck coefficient, σ is the electrical conductivity, T is the absolute temperature, κ_{lat} and κ_{el} are the lattice and electronic contributions to thermal conductivity, respectively. An ideal thermoelectric material should have a high power factor, $PF = \alpha^2\sigma$ and a low thermal conductivity in a wide range of temperatures. Various materials were studied for power generation applications, such as GeTe [4, 5], PbTe [6], Bi_2Te_3 [7], silicides [8], skutterudites [9, 10] and Heusler-type alloys [11-13]. Half-Heusler compounds constitute a group of ternary intermetallic compounds with the

general formula ABX, where A is a highly electropositive transition metal, B is a low electropositive transition metal and X is the main group element [14]. Their crystal structure consists in three interpenetrating face centered cubic (f.c.c.) sublattices and one vacant f.c.c. sublattice. Half-Heusler compounds with 18 valence electrons have been extensively studied as potential thermoelectric materials for power generation in the medium/high temperature range (800-1000 K) [15-37]. ZT of half-Heusler compounds can be improved by reducing the lattice thermal conductivity, thus several methods were investigated for increasing phonon scattering through mass fluctuation [37], phase separation [11, 26] and microstructure refinement [30,31,33,36]. Among the different families of half-Heusler compounds, it is well known that the MNiSn (M = Ti, Zr, Hf) alloys show the best thermoelectric performances [22-36]. Reported values of Seebeck coefficient and electrical conductivity of TiNiSn alloys prepared with different processing routes are quite scattered, due to the presence of residual secondary phases [24, 28]. For example, processing from the melt (arc melting, induction melting) leads to the formation of sample with multiple phases, that need long annealing to be homogenized [32].

The aim of this work is to study the effect of two different pre-processing routes (arc melting and rapid solidification [38]) on the structure and microstructure of TiNiSn half-Heusler compound. The phase selection observed after different preparation routes is described on the basis of thermodynamic arguments. Arc melted ingots and rapidly solidified flakes were post-processed by annealing and powder sintering, respectively, in order to obtain homogeneous and dense massive samples for thermoelectric characterizations. The effect of residual

secondary phases on the measured values of the Seebeck coefficient and electrical conductivity is discussed in the framework of models based on the effective medium theory. The role of grain boundary scattering on the lattice thermal conductivity is evaluated.

2. Material and methods

Polycrystalline samples of TiNiSn and $TiNi_{1.03}Sn$ were synthesized by arc-melting of elemental metals (Titanium 99.99%; Nickel 99.95%; Tin 99.995%) in Argon (5.5) atmosphere. Residual traces of oxygen in the melting atmosphere were removed by previously melting Ti and Zr getters. The ingots were flipped over and re-melted five times to ensure chemical homogeneity. On the one side, in order to obtain a single-phase sample, the arc melted ingot, wrapped in a Ta foil and sealed under vacuum in a quartz tube, was annealed for three weeks at 1123 K and then for ten days at 923 K. On the other side, arc melted ingots were rapidly solidified by planar flow casting (Edmund Bühler GmbH), producing fragmented ribbons. The alloy was induction melted in a boron nitride (BN) crucible under Argon (5.5) atmosphere (1 bar) and injected onto a rotating copper wheel at different peripheral wheel speed (10, 20 and 30 m/s) by an Ar overpressure of 0.2 bar with a distance between the crucible nozzle and the wheel of 0.3 mm. The rapidly solidified ribbons were ground by hand in an agate mortar, and the obtained powders were sintered by Open Die Pressing (ODP) [39]. The powders were loaded into a Fe sheath (length: 60 mm; 16.5 mm external diameter) and preheated at 973 K and sintered at 748 K for 15 min, applying a compressive load of 20 tons. For sake of clarity, the arc melted, arc

melted and annealed, rapidly solidified and as sintered samples will be named AM, AM-AN, RS and ODP, respectively.

In order to investigate the effect of secondary phases, a Ni_3Sn_4 dense ingot was prepared according to the following route: 1) alloying of the metallic elements by homogenization of the melt at 1473 K for 6 hours in a evacuated quartz ampoule, followed by two isothermal thermal treatments of 24 hours each at 1048 K and 473 K (below the peritectic and eutectic temperatures, respectively). 2) The sample obtained in the previous step was porous due to the peritectic reaction at 1068 K. Thus densification was attained by Equal Channel Angular Extrusion (ECAE), using a constant extrusion speed (10 mm/min), and channels with a diameter of 25 mm and an angle of 90°. The sample was wrapped in a copper sheath, pre-annealed at the processing temperature and extruded at 473 K and 673 K for 2 and 4 cycles, respectively. The sample was rotated of 180° after each cycle. 3) Recrystallization of the extruded ingot was performed by isothermal annealing at 873 K for 60 h.

Structural characterization was performed by X-ray diffraction (XRD) using both Bragg Brentano (Panalytical X'Pert Pro) and parallel beam (Panalytical PW3020) geometries with Cu K_α radiation (K_α = 1.5406 Å). XRD measurements were carried out on ground powders in order to remove possible effects of preferential crystallographic orientations. A Rietveld refinement [40] of the measured diffraction patterns was performed using Maud software [41].

Microstructural observations were performed by scanning electron microscopy (SEM) using a ZEISS EVO 50 XVP-LaB_6 equipped with an Oxford Instruments INCA-Energy 250 for energy-dispersive X-ray analysis (EDX).

Chemical etching was performed in Kroll's reagent (92 vol.% distilled water, 6 vol.% nitric acid and 2 vol.% hydrofluoric acid) for about 20 seconds.

Thermodynamic calculations were performed by Pandat software using the database optimized by Gürth et al. [34].

Thermal stability of the AM-AN sample was evaluated by thermogravimetric analysis, TGA (TA-Q600) under N_2 flow.

Seebeck coefficient, α, and electrical conductivity σ, were measured under He flow in the temperature range from room temperature up to 923 K, by using a custom test apparatus described in Ref. [42]. The relative error of α and σ was estimated to be around 4 % and 5 %, respectively.

The thermal conductivity κ was calculated from $\kappa = \rho D C_p$, where ρ is the mass density, D is the thermal diffusivity and C_p is the specific heat capacity. The mass density was estimated, with a relative error of 5 %, both by Archimedes principle, with a pycnometer, and using the ratio between the mass and the volume of regularly shaped samples. The thermal diffusivity was measured by laser flash method (LFA 457 MicroFlash, Netzesch, Selb, Germany) with uncertainty around 3 %. The specific heat capacity was determined using Differential Scanning Calorimetry (DSC) with a heating ramps 10 K min^{-1} in limited temperature ranges of 30 K. Each ramp was preceded and followed by a suitable isotherm in order to stabilize the DSC signal. The measurement was repeated with the empty alumina pan, a standard (sapphire) and the sample. The specific heat of the sample at different temperature was obtained by comparing the signals measured for the sample and the standard using both the "height" and the "area" methods [43].

3. Results and discussion

3.1. Effect of pre-processing on phase formation and microstructure

Figure 1(a) shows the XRD pattern of the AM ingot. The relative amount of the phases and the corresponding lattice parameters, obtained by Rietveld refinement, are reported in Table 1. The AM ingot shows the presence of TiNiSn half-Heusler phase, together with $TiNi_2Sn$ full-Heusler, Ti_6Sn_5 and Sn phases.

Figure 2(a) shows the backscattered electron image of the AM ingot. The phases identified are half-Heusler TiNiSn (1), full-Heusler $TiNi_2Sn$ (2), Ti_6Sn_5 (3), Ni_3Sn_4 (4), Ti_5Sn_3 (5), Ti (6) and Sn (7). Only the amount of the phases identified by XRD was quantified by Rietveld analysis (table 1) because the other phases were below the detection limit.

The presence of more than three phases in the AM sample indicates that the thermodynamic equilibrium was not reached, as a consequence of the complex solidification path involving a peritectic reaction [34] that is hindered by the need of a long distance diffusion. The relative amount of the phases forming upon solidification was calculated on the basis of the Scheil model, that assumes a full equilibrium in the liquid state and the absence of diffusion in the solid state. Results are shown in Figure 3(a), as a function of temperature. Most of the phases predicted by the Scheil model were experimentally observed by SEM in the AM ingot, Figure 2(a). Ti_2Sn_3, that is predicted to be the less abundant in the mixture (< 2 wt.%), was difficult to be identified by SEM. The relative amounts of the phases calculated at the end of the solidification process are compared in Figure 3(a) with the corresponding amounts obtained by the quantitative analysis

of the XRD patterns. Despite the minor phases could not be quantified by Rietveld analysis of the XRD patterns, because below the detection limit, the agreement between the calculated and experimental values for the phase fraction of TiNiSn, $TiNi_2Sn$, and Sn is rather good. However, a discrepancy between calculated and experimental values of the phase fraction for Ti_6Sn_5 and Ti_5Sn_3 is observed. In the case of Ti_6Sn_5, the experimental value is about double the calculated one, while Ti_5Sn_3, that is calculated to be more abundant than Ti_6Sn_5, is present only in traces, as shown by the SEM image in Figure 2(a). A possible explanation for this result is that the formation of Ti_5Sn_3 is kinetically hindered, due to the stoichiometry of the compound, which implies significant inter-diffusion.

Figure 3(b) shows the molar fraction of each component in the liquid phase as a function of temperature when the Scheil model is considered. Upon cooling, the liquid progressively becomes richer in Sn, rejecting Ni and Ti. Since the amount of Ti_5Sn_3 is significantly lower than expected, the Ti in excess is likely rejected by the liquid, forming a small amount of elemental Ti, as observed by the SEM image in Figure 2(a).

The XRD pattern of the RS (20 m/s) sample, Figure 1(b), shows the peaks of TiNiSn full-Heusler, together with the less intense peaks related to $TiNi_2Sn$ half-Heusler and Sn phases. The relative amount of the phases and the corresponding lattice parameters are reported in Table 1. It can be observed that, after rapid solidification, the RS sample shows a higher relative amount of the TiNiSn half-Heusler phase, together with the disappearance of the Ti_6Sn_5 phase. The SEM micrograph of Figure 2(b) shows again the presence of elemental Ti, that counterbalance the apparent excess in Ni and Sn observed by the

quantitative analysis of the XRD patterns. The presence of elemental Ti is not expected from the thermodynamic equilibrium [34] and, as discussed for the arc-melted ingot, it can be explained by kinetic reasons. Another effect of the rapid solidification process is a microstructure refinement (grain size between 0.5 μm and 5 μm), as shown by the SEM micrograph of the etched cross section of the ribbon, Figure 2(b).

Figure 4(a) shows the stable (blue line) and metastable (red line) isopleths Ni-SnTi, calculated by maintaining and suspending the $TiNi_2Sn$ phase from the database, respectively. The comparison between the two isopleths shows that an undercooling of the liquid of at least 70 K is necessary to allow the primary solidification of the TiNiSn phase. Such a degree of undercooling can be typically reached by rapid solidification [38], hindering the formation of the primary phase $TiNi_2Sn$ and allowing the solidification of the metastable liquid directly in the desired TiNiSn phase.

In order to explain the phase selection for different undercoolings of the liquid phase, the driving force for nucleation of the TiNiSn and $TiNi_2Sn$ phases from a liquid with stoichiometric composition (TiNiSn), has been calculated as a function of temperature and results are shown in Figure 4(b). When, on cooling, the value of the driving force for nucleation of a solid phase changes from negative to positive, it means that the considered phase can nucleate from a thermodynamic point of view, and it is in competition with other phases with a positive free energy. In Figure 4(b), the blue and red circles identify the values of the liquidus temperature for equilibrium $TiNi_2Sn$ (~ 1520 K) and metastable TiNiSn (~ 1445 K), respectively, as reported in Figure 4(a). The intersection between the red and

the blue lines around 1340 K identifies the temperature below which TiNiSn has a larger driving force for nucleation than $TiNi_2Sn$. In order to nucleate the TiNiSn phase directly from the liquid, this needs to be undercooled at least to ~ 1445 K , while TiNiSn becomes the most favorable nucleating phase below 1340 K. As shown by the inset of Figure 1(b), the amount of the half Heusler phase in the RS sample increases as the wheel speed increases and it is always larger than in the AM sample. As the wheel speed is raised, the degree of undercooling of the liquid increases [38], so that the driving force for nucleation of TiNiSn increases and this phase is progressively stabilized with respect to $TiNi_2Sn$.

In both AM and RS samples, the value of refined lattice parameters significantly deviates from the reference values of 5.926 Å for TiNiSn [29] and of 6.098 Å for $TiNi_2Sn$ [44]. Thus, uncontrolled solidification leads to the formation of non-stoichiometric compounds, with a larger amount of Ni in the TiNiSn cell and a lower amount of Ni in the $TiNi_2Sn$ cell, in agreement with the solvus lines in the isopleth Ni-SnTi [45]. The amount of Ni present in both half and full-Heusler phases in AM and RS samples is very close to the solubility limit around 1223 K [34], indicating that the high temperature solute content was frozen during cooling.

3.2. Post-processing of arc melted ingots and rapidly solidified ribbons

The XRD pattern of the AM-AN sample, Figure 5(a), shows only the reflections of the TiNiSn and $TiNi_2Sn$ phases, while the backscattered electron SEM image, Figure 6(a), shows traces of Ni_3Sn_4 that could not be evidenced by XRD because its amount is below the detection limit. As a consequence of the long annealing,

AM-AN sample attains equilibrium in a three phases region (TiNiSn, $TiNi_2Sn$, Ni_3Sn_4) and the lattice parameters of both TiNiSn and $TiNi_2Sn$ approach the equilibrium values, as reported in Table 1. The deviation from the single phase region can be explained by a slight deviation of the sample composition from the nominal stoichiometry, that could not be detected by EDX analysis (see Table 1-S in the Supplementary Material). The XRD pattern of ODP sample, Figure 5(b), shows diffraction peaks of the TiNiSn phase and Ni_3Sn_4, as a secondary phase. Furthermore, the ODP sample shows a slight asymmetry and a strain broadening of the diffraction peaks related to half-Heusler phase. This behavior was already observed in hot pressed TiNiSn samples and it was explained by inhomogeneous distribution of interstitial Ni in the Wyckoff position 4d in the unary cell [29]. Following this approach, we modelled the peak broadening using two half-Heusler phases (TiNiSn_1 and TiNiSn_2 as shown in Figure 1-S in the Supplementary Material): the corresponding refined lattice parameters and relative amounts are reported in Table 1. The phase TiNiSn_1 has a lattice parameter close to the equilibrium value, indicating that excess Ni was rejected during ODP, whereas the phase TiNiSn_2 shows a lattice parameter comparable to the one of the RS sample, indicating that the interstitial Ni originally present is maintained during ODP. The backscattered electron image of the ODP sample, Figure 6(c), still shows the presence of elemental Ti that was already detected in the RS ribbon.

The secondary electron images reported in Figure 6(b) and 6(d) show the AM-AN and ODP samples after chemical etching, respectively. The ODP sample, Figure 6(d), shows a finer microstructure (grain size in the 0.5-5 μm range) than

AM-AN sample (grain size in the 20-60 μm range), Figure 6(b), and it is comparable to that observed for the RS sample, Figure 2(b). The grain growth during the ODP process was limited, using sintering conditions in proximity or below the recrystallization temperature (~ 825 K), since the sample was pre-annealed at 993 K for only 5 min and pressed at 748 K for 15 min.

3.3. Thermoelectric properties

3.3.1. Electrical conductivity and Seebeck coefficient

The measured thermoelectric properties of the AM-AN (circles) and ODP (stars) samples are shown in Figure 7 as a function of temperature.

The temperature dependence of the electrical conductivity is reported in Figure 7(a). Both samples show an increasing trend with the temperature, indicating a typical semiconducting behavior. The AM-AN sample (open circles) shows a lower electrical conductivity with respect to the ODP sample (open stars) in the entire range of temperatures.

Figure 7(b) shows the temperature dependence of Seebeck coefficient (α) of the AM-AN (open circles) and ODP (open stars) samples. The Seebeck coefficient of both samples is negative in the whole temperature range, indicating that electrons are the majority carriers (n-type).

The literature values of thermopower and electrical conductivity of stoichiometric TiNiSn are quite dispersed, as already reported by Berche et al. [24] and Tang et al. [28]. As suggested by the complex solidification path (Figure 3), formation of pure single phase TiNiSn is extremely difficult, so that secondary phases are quite often present in different proportion depending on the processing method. Furthermore, the tendency of Ti to oxidize tends to deviate

the alloy composition from the nominal one, favoring the formation of secondary phases [24]. Typical secondary phases are $TiNi_2Sn$, Sn, stannides, depending on the actual composition of the alloy.

The effect of secondary phases (phase 2) on the thermoelectric properties of a matrix (phase 1) can be estimated according to different models. On the basis of the effective medium theory (EMT) [46], electrical conductivity (σ) and thermal conductivity (κ) of the phase mixture are, respectively, defined on the basis of the following equations:

$$\varphi_1 \frac{\sigma_1-\sigma_e}{\sigma_1+2\sigma_e} + \varphi_2 \frac{\sigma_2-\sigma_e}{\sigma_2+2\sigma_e} = 0 \quad (1)$$

$$\varphi_1 \frac{\kappa_1-\kappa_e}{\kappa_1+2\kappa_e} + \varphi_2 \frac{\kappa_2-\kappa_e}{\kappa_2+2\kappa_e} = 0 \quad (2)$$

where φ_1 and φ_2 are the volume fractions of phase 1 and phase 2, the subscripts 1, 2 and e refer to phase 1, phase 2 and the effective medium (i.e. the composite constituted by the mixture of phase 1 and phase 2).

An extension of the EMT is represented by the general effective medium theory (GEMT) [47], where elements of the percolation theory are considered, leading to the following equations for the electrical conductivity (σ) and thermal conductivity (κ), respectively

$$\varphi_1 \frac{\sigma_1^{1/t}-\sigma_e^{1/t}}{\sigma_1^{1/t}+A\sigma_e^{1/t}} + \varphi_2 \frac{\sigma_2^{1/t}-\sigma_e^{1/t}}{\sigma_2^{1/t}+A\sigma_e^{1/t}} = 0 \quad (3)$$

$$\varphi_1 \frac{\kappa_1^{1/t}-\kappa_e^{1/t}}{\kappa_1^{1/t}+A\kappa_e^{1/t}} + \varphi_2 \frac{\kappa_2^{1/t}-\kappa_e^{1/t}}{\kappa_2^{1/t}+A\kappa_e^{1/t}} = 0 \quad (4)$$

where $A = \frac{1-\varphi_c}{\varphi_c}$ (φ_c is the percolation threshold) and *t* is a constant related to the microstructure asymmetry in terms of connection between the grains. In the

particular case of spherical particles φ_c = 1/3 and t = 1, and equations (3) and (4) reduce to equations (1) and (2), respectively.

On the basis of the EMT, Webman, Jortner and Cohen (WJC) developed the following equation for the thermopower of a two phases mixture [48]

$$\varphi_1 \frac{\sigma_1(\alpha_e-\alpha_1)}{(2\sigma_e+\sigma_1)(2\kappa_e+\kappa_1)} + \varphi_2 \frac{\sigma_2(\alpha_e-\alpha_2)}{(2\sigma_e+\sigma_2)(2\kappa_e+\kappa_2)} = 0 \qquad (5)$$

where α_1, α_2 and α_e are the Seebeck coefficients of phase 1, phase 2 and the effective medium. All the other terms of equation (5) are same of equations (1) and (2).

The combination of the WJC and GEMT models leads to the following equation for the thermopower of a two phases mixture

$$\varphi_1 \frac{\sigma_1^{1/t}(\alpha_e^{1/t}-\alpha_1^{1/t})}{(A\sigma_e^{1/t}+\sigma_1^{1/t})(A\kappa_e^{1/t}+\kappa_1^{1/t})} + \varphi_2 \frac{\sigma_2^{1/t}(\alpha_e^{1/t}-\alpha_2^{1/t})}{(A\sigma_e^{1/t}+\sigma_2^{1/t})(A\kappa_e^{1/t}+\kappa_2^{1/t})} = 0 \qquad (6).$$

In the equations (3) and (4), related to the percolation model, the constants *A* and *t* can be determined by a fitting procedure, if the thermoelectric properties of the effective medium (σ_e or κ_e) are experimentally available over a wide range of the phase fraction φ. The same constants are then used in Eq. (6) to determined α_e.

On the basis of models described above, we calculated the temperature dependence of electrical conductivity and Seebeck coefficient, using the properties of the pure phases and the volume ratio of the phases in AM-AN and ODP samples, as determined by Rietveld refinement of the XRD patterns. Values for electrical conductivity and Seebeck coefficient for secondary phases have been taken from the literature or experimentally determined in this work. In particular, a sample of single phase Ni_3Sn_4 was prepared (the corresponding

XRD pattern is shown in Figure 2-S in the Supplementary Material). Figure 3-S in the Supplementary Material shows the temperature dependence of the measured Seebeck coefficient (a) and electrical conductivity (b), respectively, for Ni_3Sn_4 (this work), $TiNi_2Sn$ [27] and Sn [49, 50]. The low values of $|\alpha|$ and the decreasing trend of σ with temperature indicate that all these phases have, as expected, a metallic behavior. In addition, a sample with composition $TiNi_{1.03}Sn$ containing a Ni-rich half-Heusler phase (a = 5.931 Å) was prepared (the corresponding XRD pattern and temperature dependence of thermoelectric properties, α and σ, are reported in Figure 4-S and Figure 5-S, respectively, in the Supplementary Material). For AM-AN sample, the thermoelectric properties of pure TiNiSn [27] and $TiNi_2Sn$ [27] were considered. In the case of the ODP sample, the thermoelectric properties of a Ni-rich matrix (i.e. $TiNi_{1.03}Sn$) and Ni_3Sn_4 were considered.

The electrical conductivity of the phase mixtures was calculated according to EMT model, Eq. (1), and results are shown in Figure 7(a), both for the AM-AN sample (thick green line) and the ODP sample (thin red line). For the AM-AN sample, containing 2 % of $TiNi_2Sn$ as secondary phase, EMT model allows to follow the experimental values, while for the ODP sample, containing 6 % of Ni_3Sn_4 as secondary phase, the EMT model fails to fit the experimental data. The backscattered electron micrograph of ODP sample, reported in Figure 6(b), shows that the secondary phase (Ni_3Sn_4) is segregated at the grain boundaries of the half-Heusler phase matrix and tends to form a connected network. On the basis of this observation, the electrical conductivity of ODP sample was calculated considering percolation with the GEMT model, using Eq. (3). In our

case, the A and t parameters cannot be obtained by fitting because the experimental value of σ_e is available only for a single value of φ. Thus, arbitrary values, A = 5.25 (corresponding to φ_c = 16 %) and t = 2 (non spherical particles) [51], were used to find the solution of Eq. (3). The same values of the parameters *A* and *t* were also used to find the solutions of Equations (4) and (6). The calculated electrical conductivity is reported in Figure 7(a) (dashed thick red line). It turned out that calculated values assuming the GEMT model are closer to experimental data with respect to those calculated with the EMT model.

The Seebeck coefficient of the phase mixtures was calculated according to the WJC-EMT model, Eq. (5), as shown in Figure 7(b), both for the AM-AN sample (thick green line) and the ODP sample (thin red line). As in the case of the electrical conductivity, when percolation is neglected (WJC-EMT model), only the AM-AN sample shows a good agreement between the calculated and the experimental values. Calculated values closer to the experimental ones are again obtained for the ODP sample when percolation is assumed (WJC-GEMT model) using Eq. (6), as shown in Figure 7(b) (dashed thick red line).

Figure 8(a) and Figure 8(b) show the values of the Seebeck coefficient and electrical conductivity at 328 K, respectively, for stoichiometric TiNiSn as a function of the secondary phases fraction, as estimated by quantitative analysis of the XRD patterns both from this work and in the literature [26, 27, 29, 35]. The different secondary phases (Sn, Ni_3Sn_4 and $TiNi_2Sn$) in the samples considered are represented by different symbols (diamonds, circles and squares, respectively) and colors (blue, red and green, respectively). The selection of the literature data was limited to samples showing values of the lattice constant

(Table 2) close to that of stoichiometric TiNiSn [27, 29], so that the possible presence of a significant variation of the interstitial Ni content could be neglected. Figure 6-S in the Supplementary Material shows that there is not a clear dependence of the Seebeck coefficient and electrical conductivity of TiNiSn from the lattice parameter in the case of the samples selected from the literature.

The absolute value of the Seebeck coefficient clearly decreases as the total amount of secondary phases increases, due to their metallic behavior, as shown in Figure 8(a). Accordingly, the electrical conductivity raises as the total amount of secondary phases increases, Figure 8(b), even if the relationship between these two quantities is apparently less evident than the corresponding trend of the Seebeck coefficient, Figure 8(a). The larger spread of the data in Figure 8(b) can be explained by the significant difference in density of the samples (from 80 % to almost 100 %), that strongly affects the results of measurement of the electrical conductivity reported in the literature.

In Figure 8(a) and Figure 8(b), the experimental values of the Seebeck coefficient and electrical conductivity as a function of the amount of secondary phases are compared with the values calculated applying the EMT and WJC-EMT (continuous lines), GEMT and WJC-GEMT (dashed lines) models. For values of secondary phase fraction lower than 40%, the GEMT and WJC-GEMT models predict larger values of σ and lower values of $|\alpha|$, respectively, with respect to the EMT and WJC-EMT models, due to the percolating effect of the metallic secondary phases. At ~ 40% of secondary phase fraction the values calculated with the different models for each property tend to converge because the percolation threshold (φ_c = 1/3) of the EMT and WJC-EMT models was also

overcome. For both properties, the experimental values are better approximated when percolation is considered in the corresponding model (i.e., WJC-GEMT and GEMT for Seebeck coefficient and electrical conductivity, respectively). As already reported above, in the ODP sample the secondary phase Ni_3Sn_4 segregates at the grain boundaries of the half-Heusler matrix, forming a connected network. In the case of the samples containing Sn [29, 35], no information about the microstructure is given by the authors. However, since Sn has a low melting point (505 K) we can consider that it segregated at the grain boundaries "decorating" the grains of the matrix and creating a percolating path.

3.3.2 Thermal conductivity, power factor and figure of merit

Figure 7(c) shows the temperature dependence of thermal conductivity of AM-AN and ODP samples. The total thermal conductivity, κ_{tot}, was obtained from the measurement of thermal diffusivity, specific heat and density. The electronic contribution was obtained by applying the Wiedemann-Franz law ($\kappa_{el} = L\sigma T$, where $L=2.48\cdot10^{-8}$ $W\Omega K^{-2}$ is the Lorenz's constant, σ is the electrical conductivity, T is the absolute temperature), while the lattice contribution, κ_{lat}, was estimated as the difference between κ_{tot} and κ_{el}.

The ODP sample shows a slightly larger electronic contribution to the thermal conductivity, κ_{el}, with respect to AM-AN sample, as a consequence of its larger electrical conductivity. On the other hand, AM-AN sample shows a significantly larger lattice contribution to the thermal conductivity, $\kappa_{lat} = \kappa_{tot} - \kappa_{el}$, that leads to a larger total thermal conductivity with respect to ODP sample. The values of κ_{tot} measured for AM-AN are among the largest reported in literature for TiNiSn samples prepared with analogous processing routes (i.e. arc/induction melting

plus annealing) [26, 52] and can be taken as a reference for a “defect-free” sample with a coarse microstructure. The lattice thermal conductivity at room temperature of the ODP sample (with an average grain size around 1 μm) normalized by the one of the AM-AN sample is about 0.62 for the as sintered sample and raises to 0.65 after thermal cycling (not shown). Bhattacharya et al. [31] estimated the effect of grain boundary scattering on the lattice thermal conductivity of TiNiSn-based half-Heusler compounds applying the model proposed by Sharp et al. [36]. It was shown that phonon scattering by grain boundaries becomes relevant only when the average grain size is below 50 μm. Considering a grain size around 1 μm, that is comparable with the one estimated for the ODP sample, the predicted lattice thermal conductivity is about 0.68 times the value of a coarse grain sample (average grain size above 50 μm), in good agreement with the experimental values obtained for the ODP sample.

The power factor of the two samples is reported in Figure 7(d) (left axis). In the AM-AN sample, the larger values of the Seebeck coefficient compensate the lower values of electrical conductivity, leading to a larger power factor with respect to ODP sample.

The overall thermoelectric performance is represented by the figure of merit, ZT, as reported in Figure 7(d) (right axis). Around 850 K the figure of merit of the AM-AN sample shows a maximum value of 0.3, that is larger than the maximum value (0.2) observed for the ODP sample. The larger value of ZT for the AM-AN sample is due to the larger power factor, that compensate the larger thermal conductivity. The maximum values of ZT obtained for the AM-AN sample is in

agreement with typical values reported in literature (about 0.30-0.35) for nearly single TiNiSn phase [26, 52].

3.3.3 Thermal cycling

Thermoelectric properties (Seebeck coefficient, electrical conductivity and power factor) of the AM-AN sample were measured upon thermal cycling from room temperature up to 900 K under helium flow, as shown in Figure 9.

Between room temperature and about 750 K, the absolute value of the Seebeck coefficient during the second cycle decreases with respect to the first one, while electrical conductivity increases. Above 750 K, both Seebeck coefficient and electrical conductivity of the second cycle overlap the values measured during the first cycle.

The structure of crystal phases present at the surface of the AM-AN sample after the first cycle of measurement was characterized by parallel beam XRD, using a constant angle of incident beam $\omega = 3°$. The obtained diffraction pattern is reported in Figure 7-S in the Supplementary Material and it shows only the reflections of TiO_2 and Ni_3Sn_4 phases, that cannot be detected when the measurement is performed with Bragg-Brentano geometry (not shown), indicating the formation of a surface layer of titanium oxide and Ni_3Sn_4. According to the TGA measurement (see Figure 8-S in the Supplementary Material), the oxidation onset can be set around 700 K, since above this temperature the sample starts gaining weight. It should be noted that oxidation occurs also under inert gas flow (He and N_2 in the thermoelectric and TGA measurements, respectively) likely due to the presence of residual oxygen in the measurement apparatus.

In accordance with the XRD results, the backscattered electrons SEM image, Figure 9-S in the Supplementary Material, shows a thin layer of titanium oxide on the sample surface and the metallic phase Ni_3Sn_4 just below the oxide layer. According to Ref. [24], TiNiSn cannot dissolve oxygen, so titanium tends to oxidize leaving, below 963 K, an excess of Ni and Sn, forming the Ni_3Sn_4 phase. It must be noted that oxidation during the thermoelectric measurements occurs even if these are performed under inert gas flow, indicating the extreme sensitivity of TiNiSn to the presence of residual small amounts of oxygen. As suggested in Ref. [24], oxidation of Ti can be the cause of the presence of secondary phases in different samples of TiNiSn, explaining the extreme wide dispersion of the thermoelectric properties in the literature, as shown in Figure 8.

After polishing the surface, both the Seebeck coefficient and the electrical conductivity, measured during the third cycle, return to the values of the first cycle, indicating that the original thermoelectric properties were restored by removing the altered layer on the surface (TiO_2 and Ni_3Sn_4).

The role of the thin conductive layer of Ni_3Sn_4 on the electrical conductivity of the oxidized pellet can be evaluated by considering the presence of the two phases (i.e. Ni_3Sn_4 layer and TiNiSn bulk) as electrical resistances in parallel. The relative difference between the electrical conductivity measured in cycle 2 (σ_m) and the electrical conductivity of the thermoelectric material (σ_{TE}), measured in cycle 1, is given by:

$$\frac{\sigma_m - \sigma_{TE}}{\sigma_m} \cong \frac{\sigma_{Ni3Sn4}}{\sigma_m} \cdot \frac{A_{Ni3Sn4}}{A_m} \qquad (7)$$

where σ_{Ni3Sn4} is the electrical conductivity of pure Ni_3Sn_4, A_{Ni3Sn4} and A_m are the cross sections of the Ni_3Sn_4 layer and the whole pellet, respectively; for a

Ni_3Sn_4 layer 0.5 μm thick, the ratio between the cross sections (A_{Ni3Sn4}/A_m) is about $7 \cdot 10^{-4}$. Using the measured values of the electrical conductivity for Ni_3Sn_4 (σ_{Ni3Sn4}) and of the oxidized pellet (σ_m), the relative difference is about 91% at 300 K and drops to 4% at 623 K (see Figure 10-S in the Supplementary Material), well below the oxidation onset. In other words, the parasitic contribute of Ni_3Sn_4 becomes negligible in the temperature range (T > 700 K) where oxidation occurs and the metallic layer forms. For this reason, the electrical measurement of the oxidized pellet at high temperature can be considered reliable.

Finally, it is interesting to observe that thermal cycling does not lead to a significant variation of the power factor, Fig. 10(c), due to the opposite effect of the altered layer (TiO_2 and Ni_3Sn_4) on the Seebeck coefficient and electrical conductivity. However, oxidation and the consequent formation of secondary phases must be taken in account when designing module based on TiNiSn, because of the possible degradation of the contacts and embrittlement of the legs.

4. Conclusions

In this work, dense TiNiSn bulk samples were obtained using two different processing routes (i.e. arc melting plus annealing and rapid solidification followed by sintering). The solidification of the arc melted (AM) sample can be described by the Scheil model, that assumes complete miscibility in the liquid phase and absence of diffusion in the solid phases. Stable and metastable isopleth Ni-TiSn, obtained maintaining and suspending the $TiNi_2Sn$ phase, respectively, showed that a liquid undercooling of at least 70 K is necessary to avoid the primary solidification of $TiNi_2Sn$ and obtaining almost TiNiSn single phase, in accordance

with the experimental results of the rapidly solidified (RS) samples. Annealing of the AM sample and open die pressing of the RS sample allow to obtain homogenous and dense massive specimens (AM-AN and ODP, respectively) for thermoelectric characterization. The different thermoelectric properties of the two samples were correlated to the corresponding structural and microstructural features in the framework of a literature survey. The more metallic behavior of the ODP sample (i.e. lower absolute value of thermopower, larger electrical conductivity) with respect to the AM-AN sample was explained by the larger amount of residual metallic secondary phases. A more general analysis of selected literature data showed that electrical conductivity and Seebeck coefficient scales with the secondary phase fraction on the basis of the generalized effective medium theory (GEMT), that considers percolation of the secondary phase in the half-Heusler matrix. The lower thermal conductivity of the ODP sample with respect to the AM-AN sample was explained by the increased phonon scattering, induced by the finer microstructure obtained by rapid solidification and maintained during sintering by ODP. The AM-AN sample shows larger values of the ZT figure of merit, with a maximum of 0.3 at 850 K, with respect to the ODP sample, as a consequence of the larger power factor that compensates the larger thermal conductivity. Finally, it has been evidenced that thermal cycling upon thermoelectric measurements induces surface oxidation around 700-750 K with formation of TiO_2 and Ni_3Sn_4.

Acknowledgements

Alberto Castellero and Francesco Aversano thank University of Turin and Compagnia di Sanpaolo for financial support (Project n. CSTO162398). The authors also thank Dr. G. Fiore (University of Turin) and Mr. E. Bassani (CNR-ICMATE, Unità di Lecco) for the support in the arc melting and ODP processing of the samples, respectively. Prof. Peter Rogl is kindly acknowledged for providing the TDB file for the Ti-Ni-Sn system.

References

[1] F.J. DiSalvo, Thermoelectric Cooling and Power Generation, Science, 285 (1999) 703–706. https://doi.org/10.1126/science.285.5428.703

[2] D. Champier, Thermoelectric generators: A review of applications, Energy Conv. Manag. 140 (2017) 167–181. https://doi.org/10.1016/j.enconman.2017.02.070.

[3] M. Zebarjadi, K. Esfarjani, M.S. Dresselhaus, Z.F. Ren, G. Chen, Perspectives on Thermoelectrics: From Fundamentals to Device Applications, Energy Environ. Sci. 5 (2012) 5147–5162. https://doi.org/10.1039/C1EE02497C.

[4] N. Madar, T. Givon, D. Mogilyanski, Y. Gelbstein, High thermoelectric potential of Bi_2Te_3 alloyed GeTe-rich phases, J. Appl. Phys. 120 (2016) 035102. https://doi.org/10.1063/1.4958973.

[5] Y. Gelbstein, J. Davidow, E. Leshem, O. Pinshow, S. Moisa, Significant lattice thermal conductivity reduction following phase separation of the highly efficient $Ge_xPb_{1-x}Te$ thermoelectric alloys, Phys. Status Solidi B 251 (2014) 1431-1437. https://doi.org/10.1002/pssb.201451088.

[6] T. Parashchuk, Z. Dashevsky, K. Wojciechowski, 2019. Feasibility of a high stable PbTe: In semiconductor for thermoelectric energy applications. J. Appl. Phys. 125, 245103. https://doi.org/10.1063/1.5106422.

[7] I.T. Witting, T.C. Chasapis, F. Ricci, M. Peters, N.A. Heinz, G. Hautier, G.J. Snyder, 2019. The Thermoelectric Properties of Bismuth Telluride. Adv. Electron. Mater. 5, 1800904. https://doi.org/10.1002/aelm.201800904.

[8] Y. Sadia, N. Madar, I. Kaler, Y. Gelbstein, Thermoelectric properties in the quasi-binary $MnSi_{1.73}$-$FeSi_2$ system, J. Electron. Mater. 44 (2015) 1637. https://doi.org/10.1007/s11664-014-3500-z.

[9] G. Rogl, P. Rogl, Skutterudites, a Most Promising Group of Thermoelectric Materials, Curr. Opin. Green Sustain. Chem. 4 (2017) 50–57. https://doi.org/10.1016/j.cogsc.2017.02.006.

[10] F. Aversano, S. Branz, E. Bassani, C. Fanciulli, A. Ferrario, S. Boldrini, M. Baricco and A. Castellero, Effect of rapid solidification on the synthesis and thermoelectric properties of Yb-filled Co_4Sb_{12} skutterudite, J. Alloys Compd. 796 (2019) 33-41. https://doi.org/10.1016/j.jallcom.2019.04.337.

[11] O. Appel, T. Zilber, S. Kalabukhov, O. Beeri, Y. Gelbstein, Morphological Effects on the Thermoelectric Properties of $Ti_{0.3}Zr_{0.35}Hf_{0.35}Ni_{1+\delta}Sn$ Alloys Following Phase Separation, J. Mater. Chem. C 3 (2015) 11653–11659. https://doi.org/10.1039/C5TC03214H.

[12] C. Felser, A. Hirohata (Eds.), Heusler Alloys: Properties, Growth, Applications, Springer, Cham, 2016.

[13] F. Aversano, A. Ferrario, S. Boldrini, C. Fanciulli, M. Baricco, and A. Castellero, Thermoelectric Properties of TiNiSn Half Heusler Alloy Obtained by

Rapid Solidification and Sintering, J. Mater. Eng. Perform. 27 (2018) 6306–6313. https://doi.org/10.1007/s11665-018-3735-6.

[14] H. Hohl, A. P. Ramirez, C. Goldmann, G. Ernst, B. Wölfing, E. Bucher, New compounds with MgAgAs-type structure: NbIrSn and NbIrSb, J. Phys.: Condens. Matter 10 (1998) 7843-7850. https://doi.org/10.1088/0953-8984/10/35/016.

[15] M.A.A. Mohamed, E.M.M. Ibrahim, N.P. Rodriguez, S. Hampel, B. Büchner, G. Schierning, K. Nielsch, R. He, Tuning of the electronic and phononic properties of NbFeSb half-Heusler compound by Sn/Hf co-doping, Acta Mater. 196 (2020) 669-676. https://doi.org/10.1016/j.actamat.2020.07.028.

[16] K. Gofryk, D. Kaczorowski, T. Plackowski, A. Leithe-Jasper, Y. Grin, 2011. Magnetic and Transport Properties of Rare-Earth-Based Half-Heusler Phases RPdBi: Prospective Systems for Topological Quantum Phenomena. Phys. Rev. B. 84, 035208. https://doi.org/10.1103/PhysRevB.84.035208.

[17] O. Pavlosiuk, X. Fabreges, A. Gukasov, M. Meven, D. Kaczorowski, P. Wis´niewski, Magnetic Structures of REPdBi Half-Heusler Bismuthides (RE = Gd, Tb, Dy, Ho, Er), Physica B 536 (2018) 56-59. https://doi.org/10.1016/j.physb.2017.10.062.

[18] J.-W.G. Bos, R.A. Downie, 2014. Half-Heusler Thermoelectric: A Complex Class of Materials. J. Phys.: Condens. Matter. 26, 433201. https://doi.org/10.1088/0953-8984/26/43/433201.

[19] R. Gautier, X. Zhang, L. Hu, L. Yu, Y. Lin, T.O.L. Sunde, D. Chon, K.R. Poeppelmeier, and A. Zunger, Prediction and Accelerated Laboratory Discovery

of Previously Unknown 18-Electron ABX Compounds, Nat. Chem. 7 (2015) 308–316. https://doi.org/10.1038/nchem.2207.

[20] T. Zhu, C. Fu, H. Xie, Y. Liu, X. Zhao, 2015. High Efficiency Half-Heusler Thermoelectric Materials for Energy Harvesting. Adv. Energy Mater. 5, 1500588. https://doi.org/10.1002/aenm.201500588.

[21] L. Huang, Q. Zhang, B. Yuan, X. Lai, X. Yan, Z. Ren, Recent Progress in Half-Heusler Thermoelectric Materials, Mater. Res. Bull. 76 (2016) 107–112. https://doi.org/10.1016/j.materresbull.2015.11.032.

[22] F.G. Aliev, A.I. Belogorokhov, N.B. Brandt, V.V. Kozyrkov, R.V. Skolozdra, Y.V. Stadnyk, Optical Properties of the Vacancy MNiSn Lattices (M = Ti, Zr, Hf), JETP Lett. 47 (1988) 184–187.

[23] M. Gürth, G. Rogl, V.V. Romaka, A. Grytsiv, E. Bauer, P.Rogl, Thermoelectric high ZT half-Heusler alloys $Ti_{1-x-y}Zr_xHf_yNiSn$ ($0 \leq x \leq 1$; $0 \leq y \leq 1$), Acta Mater. 104 (2016) 210-222. https://doi.org/10.1016/j.actamat.2015.11.022.

[24] A. Berche, P. Jund, Oxidation of half-Heusler NiTiSn materials: Implications for thermoelectric applications, Intermetallics 92 (2018) 62-71. https://doi.org/10.1016/j.intermet.2017.09.014.

[25] S. W. Kim, Y. Kimura, and Y. Mishima, High temperature thermoelectric properties of TiNiSn-based half-Heusler compounds, Intermetallics, 15 (2007) 349–356. https://doi.org/10.1016/j.intermet.2006.08.008.

[26] J.E. Douglas, C.S. Birkel, N. Verma, V.M. Miller, M.-S. Miao, G.D. Stucky, T.M. Pollock, R. Seshadri, 2014. Phase Stability and Property Evolution of

Biphasic Ti-Ni-Sn Alloys for Use in Thermoelectric Applications. J. Appl. Phys. 115, 043720. https://doi.org/10.1063/1.4862955.

[27] R.A. Downie, R.I. Smith, D.A. MacLaren, J.-W.G. Bos, Metal Distributions, Efficient n-Type Doping, and Evidence for in-Gap States in $TiNiM_ySn$ (M = Co, Ni, Cu) half-Heusler nanocomposites, Chem. Mater. 27 (2015) 2449–2459. https://doi.org/10.1021/cm5045682.

[28] Y. Tang, X. Li, L.H.J. Martin, E. Cuervo Reyes, T. Ivas, C. Leinenbach, S. Anand, M. Peters, G.J. Snyder, C. Battaglia, Impact of Ni Content on the Thermoelectric Properties of Half-Heusler TiNiSn, Energy Environ. Sci. 11 (2018) 311–320. https://doi.org/10.1039/C7EE03062B.

[29] S.A. Barczak, J. Buckman, R.I. Smith, A.R. Baker, E. Don, I. Forbes, J.-W.G. Bos, 2018. Impact of Interstitial Ni on the Thermoelectric Properties of the Half-Heusler TiNiSn. Materials. 11, 536. https://doi.org/10.3390/ma11040536.

[30] M. Schrade, K. Berland, S.N.H. Eliassen, M.N. Guzik, C. Echevarria-Bonet, M.H. Sørby, P. Jenus, B.C. Hauback, R. Tofan, A.E. Gunnæs, C. Persson, O.M. Løvvik, T.G. Finstad, 2017. The Role of Grain Boundary Scattering in Reducing the Thermal Conductivity of Polycrystalline XNiSn (X = Hf, Zr, Ti) Half-Heusler Alloys. Sci. Rep. 7, 13760. https://doi.org/10.1038/s41598-017-14013-8.

[31] S. Bhattacharya, M.J. Skove, M. Russell, T.M. Tritt, Y. Xia, V. Ponnambalam, S.J. Poon, N. Thadhani, 2008. Effect of Boundary Scattering on the Thermal Conductivity of TiNiSn-Based Half-Heusler Alloys. Phys. Rev. B. 77, 184203. https://doi.org/10.1103/PhysRevB.77.184203.

[32] B.A. Cook, J.L. Harringa, Z.S. Tan, W.A. Jesser, TiNiSn: A Gateway to the (1,1,1) Intermetallic Compounds, in 15th International Conference on Thermoelectrics, 26–29 March 1996 (IEEE, Pasadena, CA, 1996), pp. 122–127

[33] G. Rogl, S. Ghosh, L. Wang, J. Bursik, A. Grytsiv, M. Kerber, E. Bauer, R. C. Mallik, X.-Q. Chen, M. Zehetbauer, P.Rogl, Half-Heusler alloys: Enhancement of ZT after severe plastic deformation (ultra-low thermal conductivity), Acta Mater. 183 (2020) 285-300. https://doi.org/10.1016/j.actamat.2019.11.010.

[34] M. Gurth, A. Grytsiv, J. Vrestal, V.V. Romaka, G. Giester, E. Bauer, P. Rogl, On the Constitution and Thermodynamic Modelling of the System Ti-Ni-Sn, RSC Adv. 5 (2015) 92270–92291. https://doi.org/10.1039/C5RA16074J.

[35] T. Berry, S. Ouardi, G. H. Fecher, B. Balke, G. Kreiner, G. Auffermann, W. Schnelle, C. Felser, Improving thermoelectric performance of TiNiSn by mixing MnNiSb in the half-Heusler structure, Phys. Chem. Chem. Phys. 19 (2017) 1543-1550. https://doi.org/10.1039/C6CP06859F.

[36] J.W. Sharp, S.J. Poon, H.J. Goldsmid, Boundary Scattering and the Thermoelectric Figure of Merit, Phys. Status Solidi A 187 (2001) 507-516. https://doi.org/10.1002/1521-396X(200110)187:2<507::AID-PSSA507>3.0.CO;2-M.

[37] C. Fu, H. Xie, T.J. Zhu, J. Xie, X.B. Zhao, 2012. Enhanced phonon scattering by mass and strain field fluctuations in Nb substituted FeVSb half-Heusler thermoelectric materials. J. Appl. Phys. 112, 124915. https://doi.org/10.1063/1.4772605.

[38] M. Baricco, E. Bosco, E. Olivetti, M. Palumbo, P. Rizzi, A. Stantero, and L. Battezzati, Rapid Solidification of Alloys, Int. J. Mater. Prod. Technol. 20 (2004) 358–376. https://doi.org/10.1504/IJMPT.2004.004762.

[39] S. Ceresara, C. Fanciulli, F. Passaretti, D. Vasilevskiy, Texturing of $(Bi_{0.2}Sb_{0.8})_2Te_3$ Nanopowders by Open Die Pressing, J. Electron. Mater. 42 (2013) 1529–1534. https://doi.org/10.1007/s11664-012-2313-1.

[40] R.A. Young, The Rietveld method, Oxford University Press, New York, 1993.

[41] MAUD, Materials Analysis Using Diffraction. http://maud.radiographema.com, 2020 (accessed 15 January 2020).

[42] S. Boldrini, A. Famengo, F. Montagner, S. Battiston, S. Fiameni, M. Fabrizio, and S. Barison, Test rig for High-Temperature Thermopower and Electrical Conductivity Measurements, J. Electron. Mater. 42 (2013) 1319–1323. https://doi.org/10.1007/s11664-012-2437-3.

[43] R.F. Speyer, Thermal Analysis of Materials, Marcel Dekker Inc., New York, 1994.

[44] International Center for Diffraction Data, Powder Diffraction File 00-052-0905

[45] N. Verma, J.E. Douglas, S. Krämer, T.M. Pollock, R. Seshadri, C.G. Levi, Microstructure Evolution of Biphasic $TiNi_{1+x}Sn$ Thermoelectric Materials, Metall. Mater. Trans. A, 47 (2016) 4116-4127. https://doi.org/10.1007/s11661-016-3549-9.

[46] R. Landauer, The Electrical Resistance of Binary Metallic Mixtures, J. Appl. Phys. 23 (1952) 779-784. https://doi.org/10.1063/1.1702301.

[47] D.S. McLachlan, 1987. An equation for the conductivity of binary mixtures with anisotropic grain structures. J. Phys. C: Solid State Phys. 20, 865. https://doi.org/10.1088/0022-3719/20/7/004.

[48] I. Webman, J. Jortner, M.H. Cohen, Thermoelectric power in inhomogeneous materials, Phys. Rev. B 16 (1977) 2959-2964. https://doi.org/10.1103/PhysRevB.16.2959

[49] P. Fiflis, L. Kirsch, D. Andruczyk, D. Curreli, D.N. Ruzic, Seebeck coefficient measurements on Li, Sn, Ta, Mo, and W, J. Nucl. Mater. 438 (2013) 224-227. https://doi.org/10.1016/j.jnucmat.2013.03.043.

[50] C.J. Smithells, E.A. Brandes (Eds.), Metals Reference Book, Butterworths, London & Boston, 1976, p. 943.

[51] J.-B. Vaney, A. Piarristeguy, V. Ohorodniichuck, O. Ferry, A. Pradel, E. Alleno, J. Monnier, E. B. Lopes, A. P. Gonçalves, G. Delaizir, C. Candolfi, A. Dauscher, B. Lenoir, Effective medium theory based modeling of the thermoelectric properties of composites: comparison between predictions and experiments in the glass–crystal composite system $Si_{10}As_{15}Te_{75}$–$Bi_{0.4}Sb_{1.6}Te_3$, J. Mater. Chem. C 3 (2015) 11090-11098. https://doi.org/10.1039/C5TC02087E.

[52] T. Katayama, S.W. Kim, Y. Kimura, Y. Mishima, The effects of quaternary additions on thermoelectric properties of TiNiSn-based half Heusler alloys, J. Electron. Mater. 32 (2003) 1160-1165. https://doi.org/10.1007/s11664-003-0006-5.

Tables Captions

Table 1. AM, RS, AM-AN and ODP samples: density, crystalline phases, relative amount and lattice parameters of the phases.

Table 2. Selected samples from the literature [26, 27, 29, 35]: relative density, secondary phases, relative amount and lattice parameters of the phases.

Table 1

Sample	Density (g/cm^3)	Phases	Relative amount (wt.%)	Lattice parameter (Å)
AM	_	TiNiSn	62	5.949(1)
		$TiNi_2Sn$	26	6.075(2)
		Ti_6Sn_5	9	-
		Sn	3	-
RS (20 m/s)	_	TiNiSn	85	5.950(6)
		$TiNi_2Sn$	11	6.061(3)
		Sn	4	-
AM-AN	6.78	TiNiSn	98	5.928(4)
		$TiNi_2Sn$	2	6.103(7)
ODP	6.82	TiNiSn_1	58	5.926(8)
		TiNiSn_2	36	5.943(4)
		Ni_3Sn_4	6	-

Table 2

Ref.	Relative density (%)	Secondary phase	Relative amount (wt.%)	TiNiSn lattice parameter (Å)
26	93	$TiNi_2Sn$	2	5.9292
27	80	-	0	5.9297
29	88	Sn	2	5.9304
35	-	Sn	8	5.9285

Figures Captions

Figure 1. X-ray diffraction patterns of arc melted (AM) ingot (a) and rapidly solidified (RS) ribbon obtained with a wheel speed of 20 m/s (b). The black dots represent the experimental patterns, the red line represents the fitted pattern, and the blue line represents the difference between the experimental and fitted patterns. The inset in (b) shows the relative amount of the TiNiSn half Heusler phase as a function of the wheel speed.

Figure 2. Backscattered electrons SEM micrographs of the arc melted (AM) ingot (a) and the rapidly solidified (RS) ribbon obtained with a wheel speed of 20 m/s (b). The labels indicate the phases identified by EDS analysis: TiNiSn (1), $TiNi_2Sn$ (2), Ti_6Sn_5 (3), Ni_3Sn_4 (4), Ti_5Sn_3 (5), Ti (6) and Sn (7).

Figure 3. (a) Phase fraction as function of the temperature below the liquidus. The points represent the experimental values obtained at room temperature by Rietveld refinement of the X-ray diffraction pattern of the AM ingot in Figure 1(b). The lines represent the calculated values on the basis the Scheil model. (b) Molar fraction of the pure components in the liquid as a function of temperature according to the Scheil model.

Figure 4. (a) Stable (red line) and metastable (blue line) isopleths Ni-SnTi obtained by maintaining and suspending the $TiNi_2Sn$ phase, respectively. (b)

Driving force for nucleation (free energy) of $TiNi_2Sn$ and TiNiSn phases from the liquid as a function of temperature.

Figure 5. X-ray diffraction patterns of the annealed arc melted ingot, AM-AN, (a), and the as sintered ODP sample (b). The black dots represent the experimental patterns, the red line represents the fitted pattern, and the blue line represents the difference between the experimental and fitted patterns.

Figure 6. Backscattered electrons SEM micrographs of the annealed arc melted ingot, AM-AN, (a) and the as sintered ODP sample (b). Secondary electrons SEM micrographs of the etched annealed arc melted ingot, AM-AN, (c) and the as sintered ODP sample (d). The labels indicate the secondary phases identified by EDX analysis: $TiNi_2Sn$ (2), Ni_3Sn_4 (4), Ti (6).

Figure 7. Temperature dependence of the electrical conductivity (a), Seebeck coefficient (b), thermal conductivity (c), power factor and figure of merit (d). Symbols represent the experimental values of the different thermoelectric properties measured for AM-AN (green circles) and ODP (red stars) samples. Lines represent the calculated electrical conductivity, (a), and Seebeck coefficient, (b), for AM-AN (thick green continuous lines) and ODP (thin red continuous lines and thick red dashed lines) samples on the basis of different models, as describe in the text.

Figure 8. Seebeck coefficient (a) and electrical conductivity (b) as a function of the secondary phase amount at 328 K. Symbols represent experimental values of the thermoelectric properties taken from the literature and this work. Solid symbols with different shapes and colors refer to samples containing different types of secondary phases. Open symbols refer to pure reference samples (i.e. TiNiSn and $TiNi_{1.03}Sn$). Continuous lines with different thickness and colors represent the calculated thermoelectric properties as a function of the amount of each secondary phase, on the basis of the effective medium theory (EMT, Eq. 1, WJC-EMT, Eq. 5). Dashed lines with different thickness and colors represent the calculated thermoelectric properties as a function of the amount of each secondary phase, on the basis of the generalized effective medium theory (GEMT, Eq. 3, WJC-GEMT, Eq. 6) considering percolation.

Figure 9. Temperature dependence of the Seebeck coefficient (a), electrical conductivity (b) and power factor (c) measured during three thermal cycles. Black open circles and red open triangles represent the thermoelectric properties measured upon two consecutive cycles. The green crosses represent the same thermoelectric properties measured in the third cycle after polishing the sample surface.

Figure 1

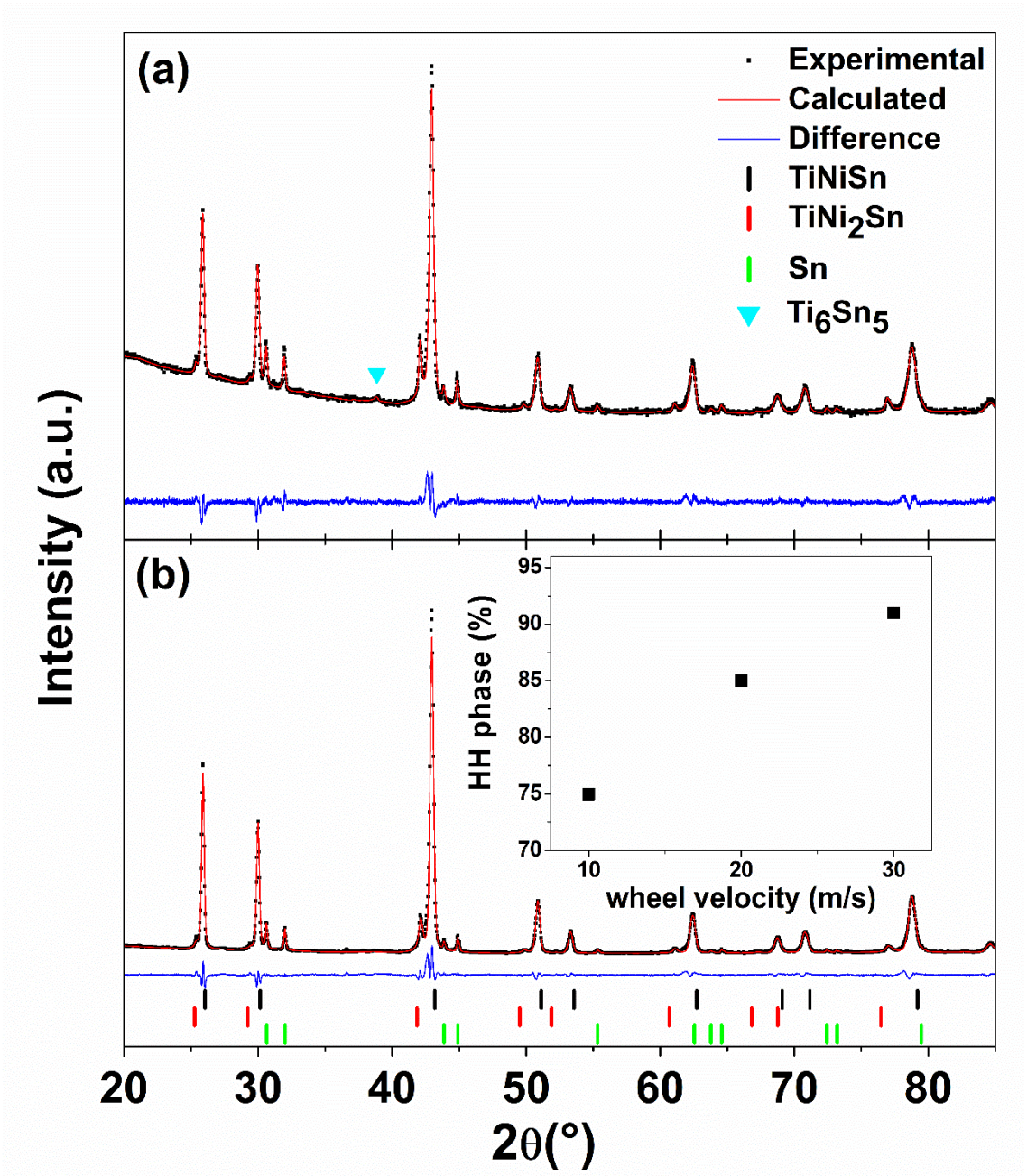
(a)
Experimental
Calculated
Difference
TiNiSn
TiNi2Sn
Sn
Ti6Sn5
(b)
HH phase (%)
wheel velocity (m/s)
Intensity (a.u.)
2θ(°)

Figure 2

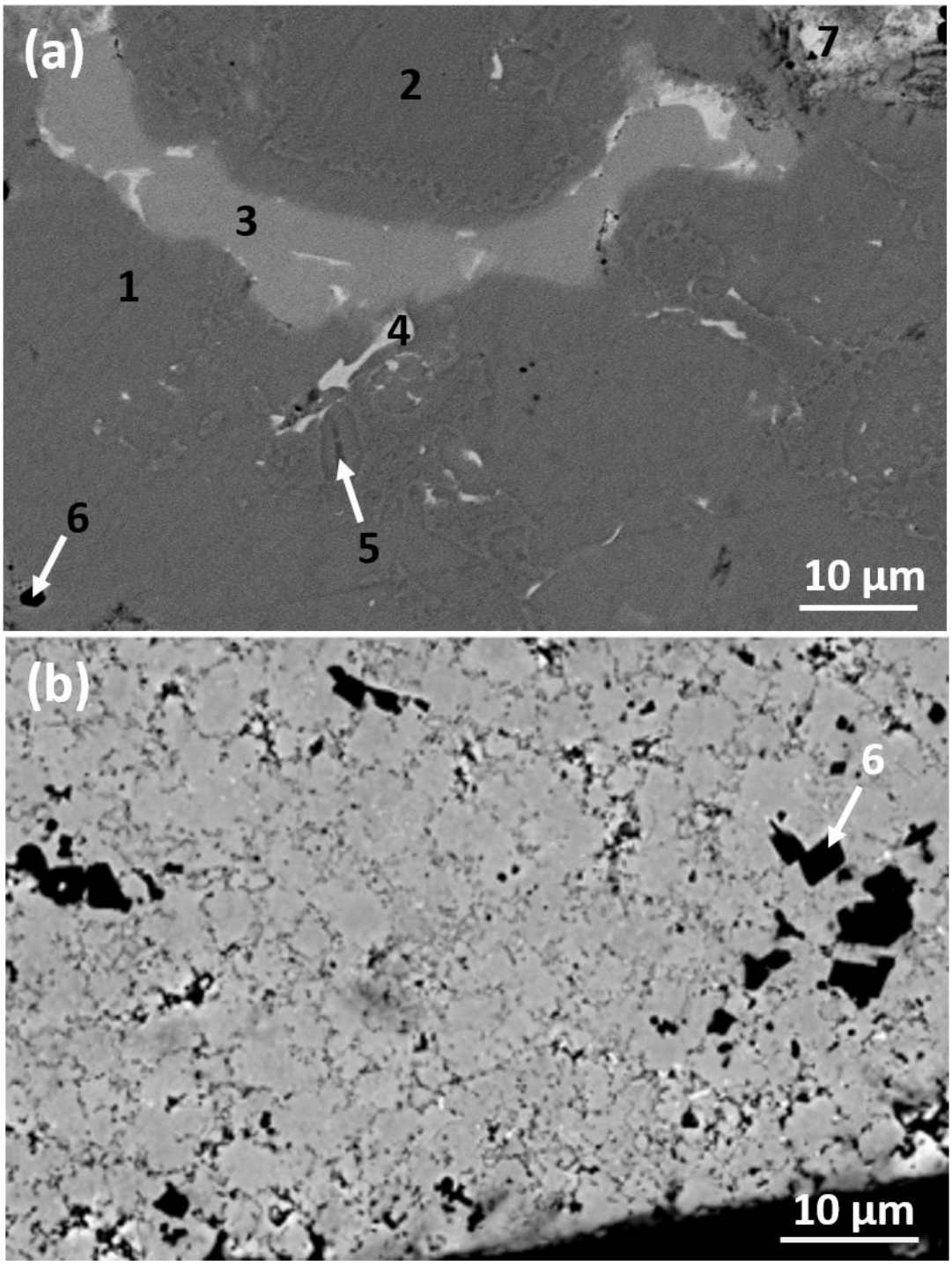

Figure 3

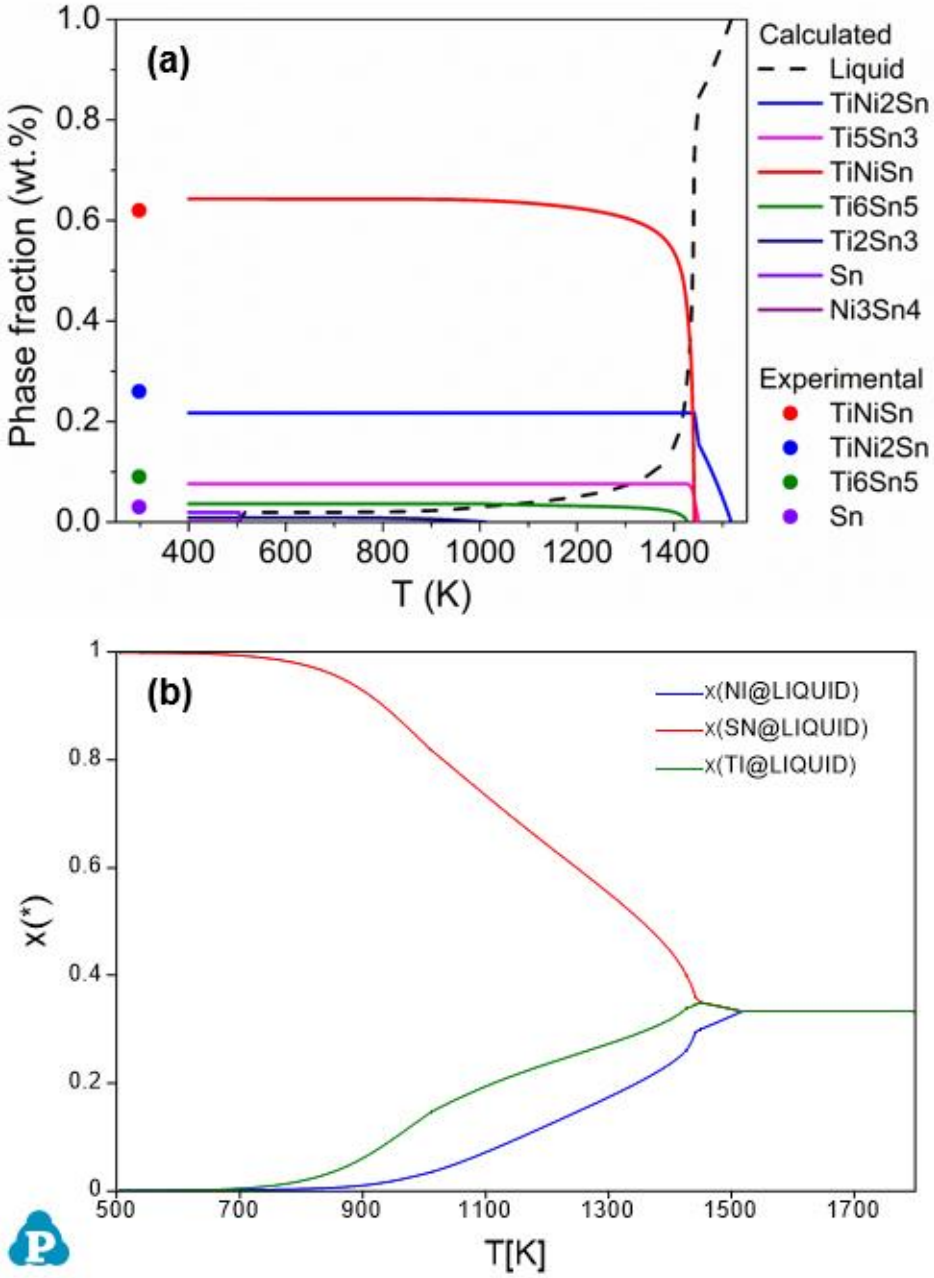
(a)
Phase fraction (wt.%)
T (K)
Calculated
Liquid
TiNi2Sn
Ti5Sn3
TiNiSn
Ti6Sn5
Ti2Sn3
Sn
Ni3Sn4
Experimental
TiNiSn
TiNi2Sn
Ti6Sn5
Sn
(b)
x(*)
T[K]
x(NI@LIQUID)
x(SN@LIQUID)
x(TI@LIQUID)

Figure 4

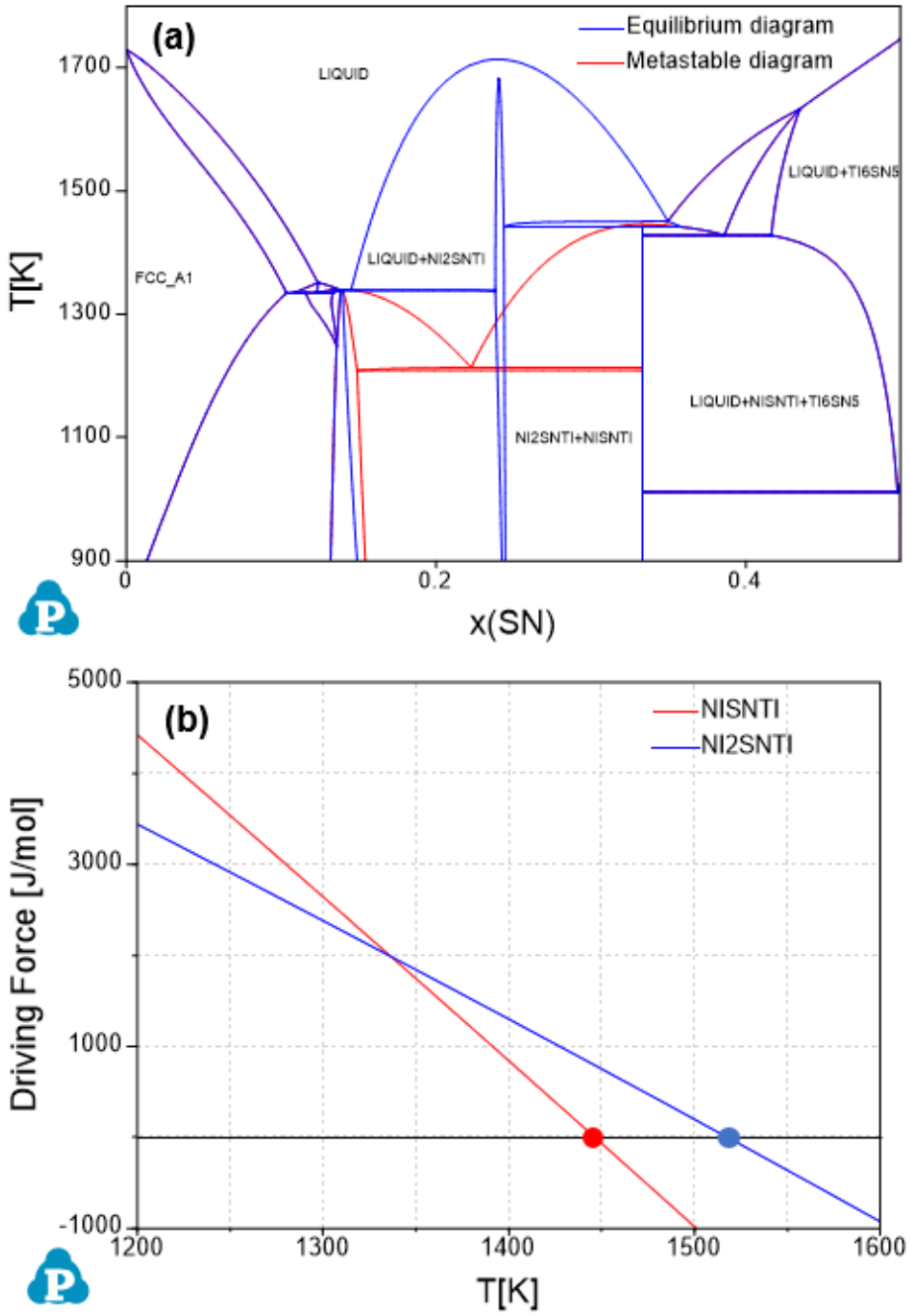
(a)
Equilibrium diagram
Metastable diagram
LIQUID
LIQUID+TI6SN5
LIQUID+NI2SNTI
FCC_A1
LIQUID+NISNTI+TI6SN5
NI2SNTI+NISNTI
T[K]
x(SN)
1700
1500
1300
1100
900
0
0.2
0.4
(b)
NISNTI
NI2SNTI
Driving Force [J/mol]
T[K]
5000
3000
1000
-1000
1200
1300
1400
1500
1600

Figure 5

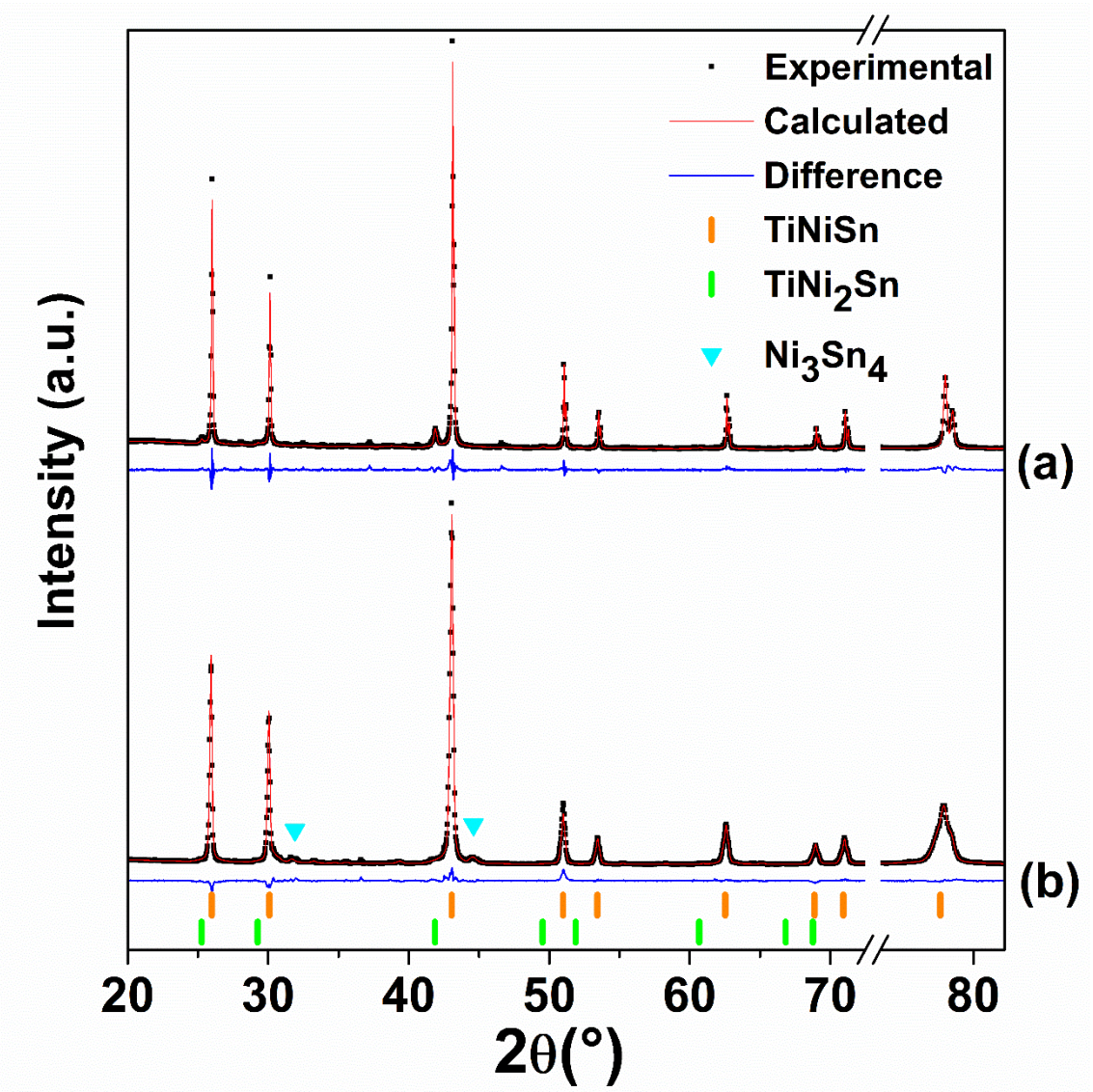
Experimental
Calculated
Difference
TiNiSn
TiNi2Sn
Ni3Sn4
(a)
(b)
Intensity (a.u.)
20
30
40
50
60
70
80
2θ(°)

Figure 6

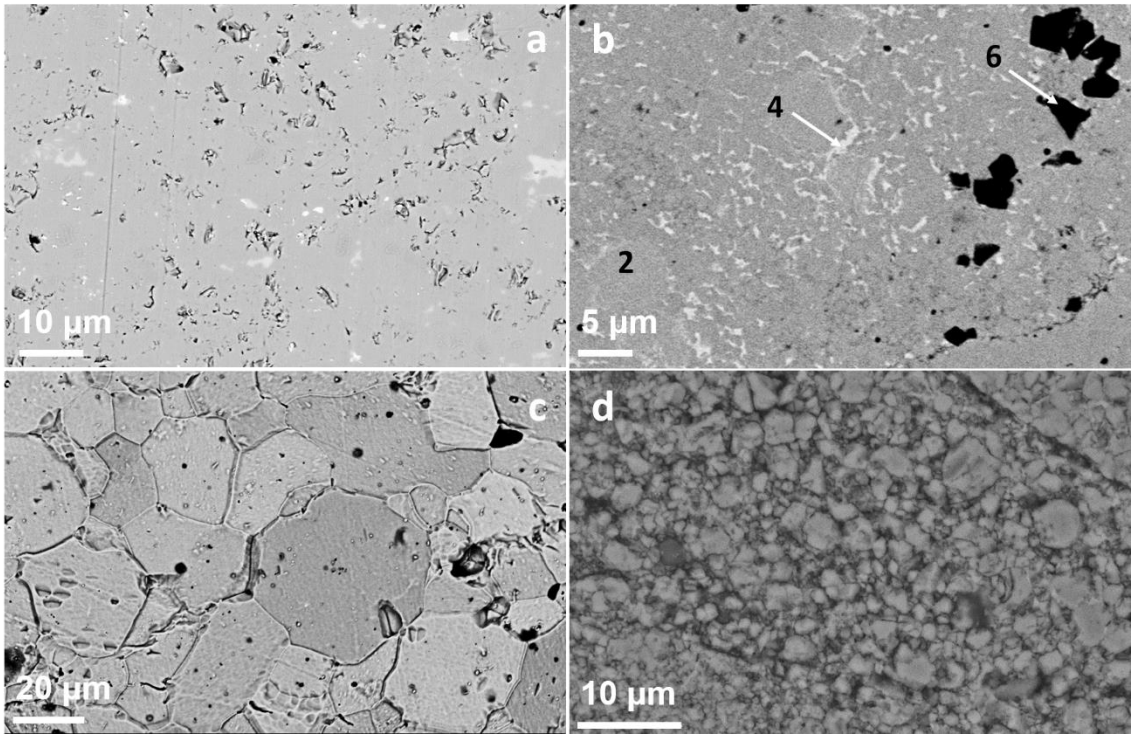

Figure 7

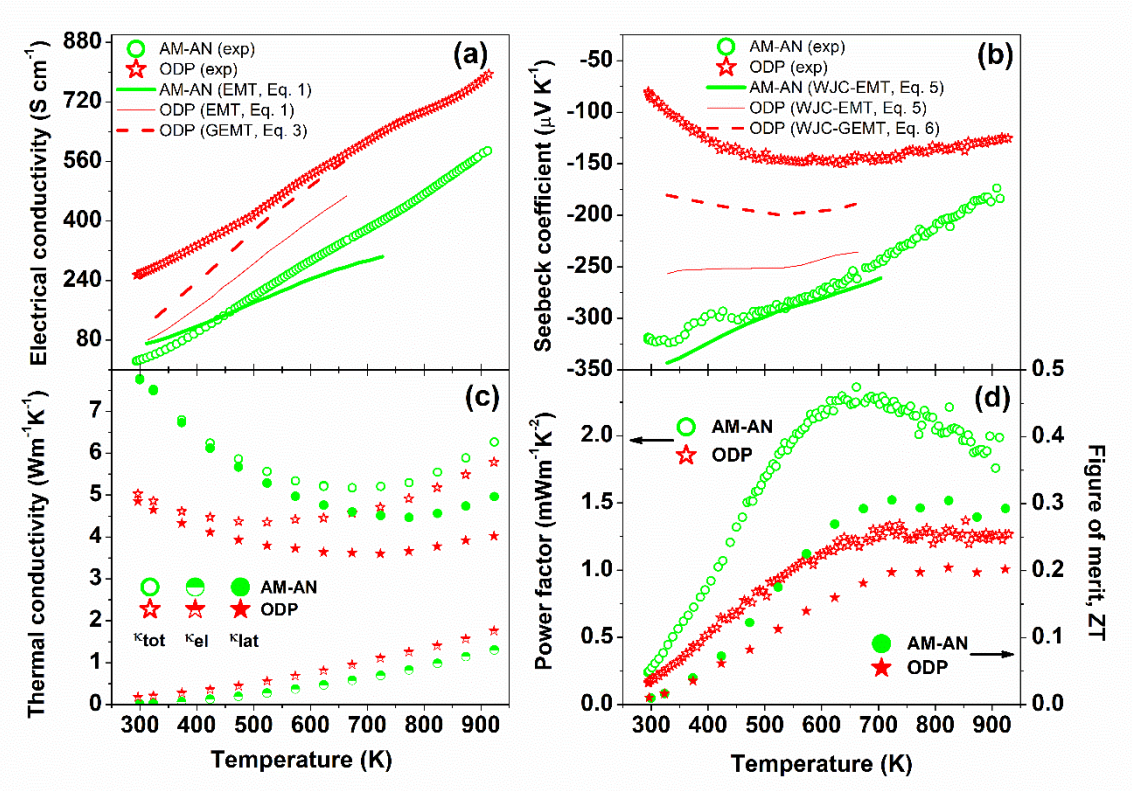
(a)
AM-AN (exp)
ODP (exp)
AM-AN (EMT, Eq. 1)
ODP (EMT, Eq. 1)
ODP (GEMT, Eq. 3)
Electrical conductivity (S cm-1)
(b)
AM-AN (exp)
ODP (exp)
AM-AN (WJC-EMT, Eq. 5)
ODP (WJC-EMT, Eq. 5)
ODP (WJC-GEMT, Eq. 6)
Seebeck coefficient (μV K-1)
(c)
AM-AN
ODP
κtot κel κlat
Thermal conductivity (Wm-1K-1)
(d)
AM-AN
ODP
AM-AN
ODP
Power factor (mWm-1K-2)
Figure of merit, ZT
Temperature (K)
Temperature (K)

Figure 8

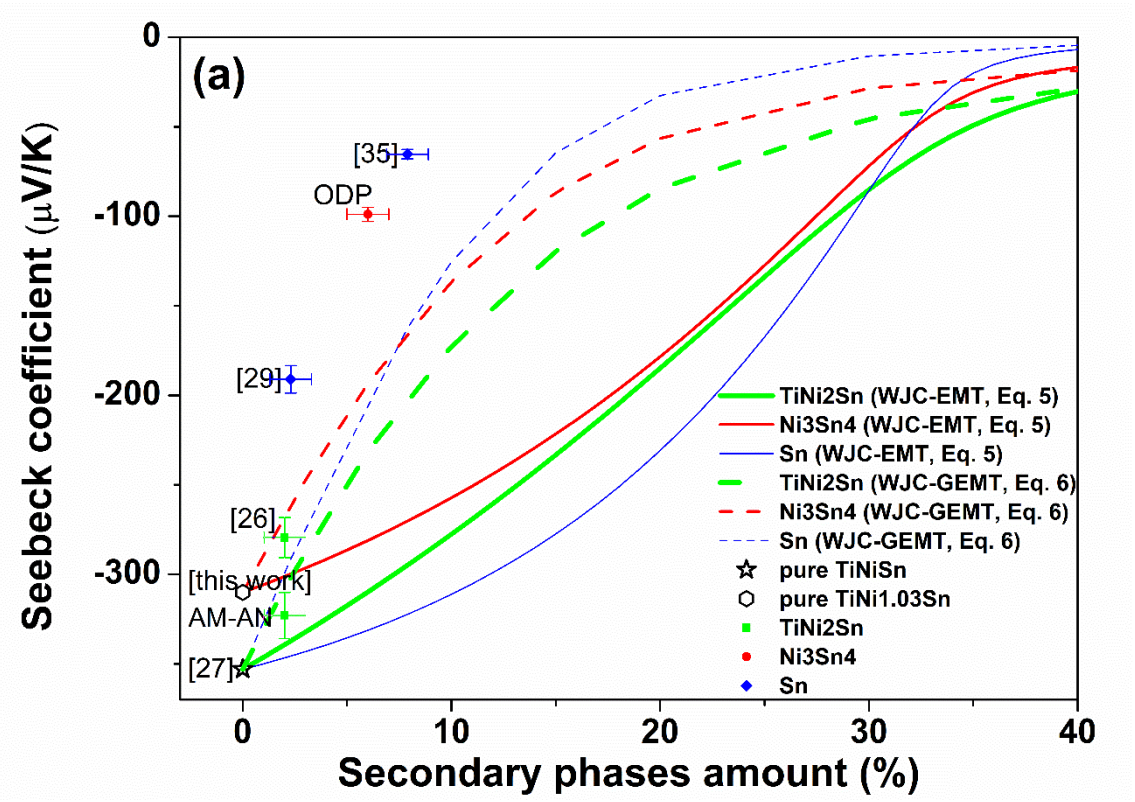
(a)
Seebeck coefficient (μV/K)
0
-100
-200
-300
[35]
ODP
[29]
[26]
[this work]
AM-AN
[27]
TiNi2Sn (WJC-EMT, Eq. 5)
Ni3Sn4 (WJC-EMT, Eq. 5)
Sn (WJC-EMT, Eq. 5)
TiNi2Sn (WJC-GEMT, Eq. 6)
Ni3Sn4 (WJC-GEMT, Eq. 6)
Sn (WJC-GEMT, Eq. 6)
pure TiNiSn
pure TiNi1.03Sn
TiNi2Sn
Ni3Sn4
Sn
0
10
20
30
40
Secondary phases amount (%)

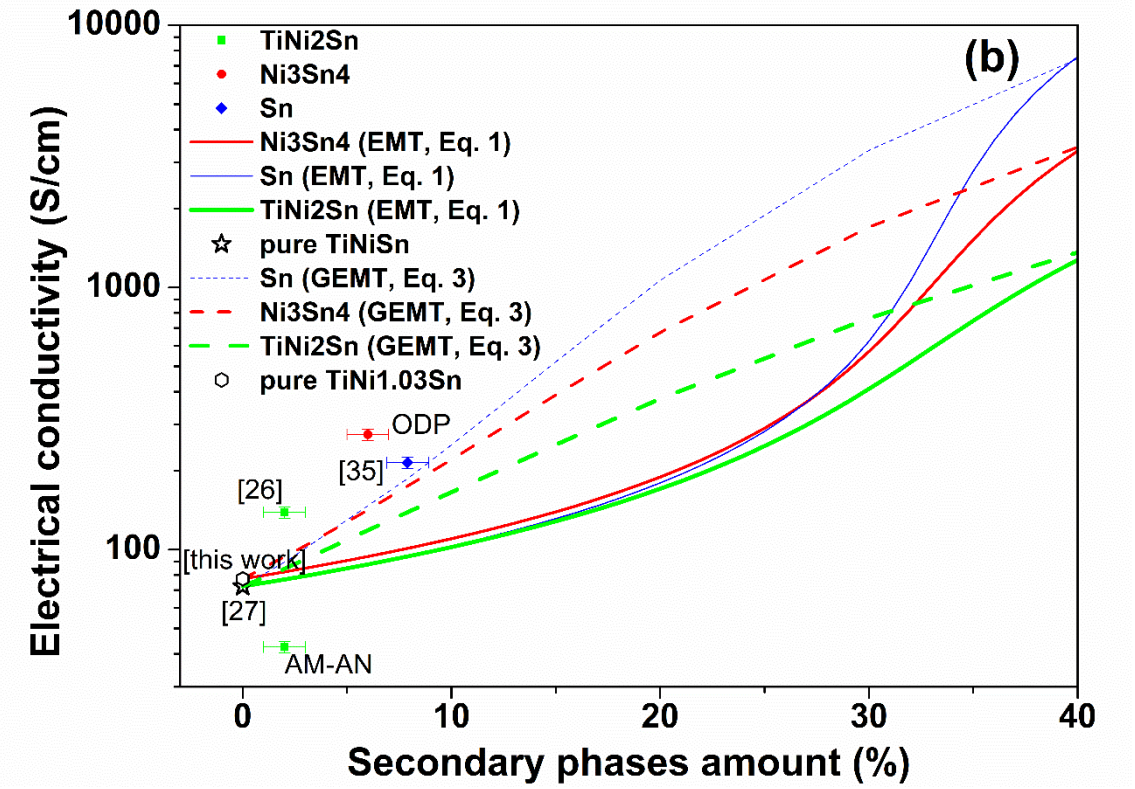
(b)
Electrical conductivity (S/cm)
10000
1000
100
TiNi2Sn
Ni3Sn4
Sn
Ni3Sn4 (EMT, Eq. 1)
Sn (EMT, Eq. 1)
TiNi2Sn (EMT, Eq. 1)
pure TiNiSn
Sn (GEMT, Eq. 3)
Ni3Sn4 (GEMT, Eq. 3)
TiNi2Sn (GEMT, Eq. 3)
pure TiNi1.03Sn
ODP
[35]
[26]
[this work]
[27]
AM-AN
0
10
20
30
40
Secondary phases amount (%)

Figure 9

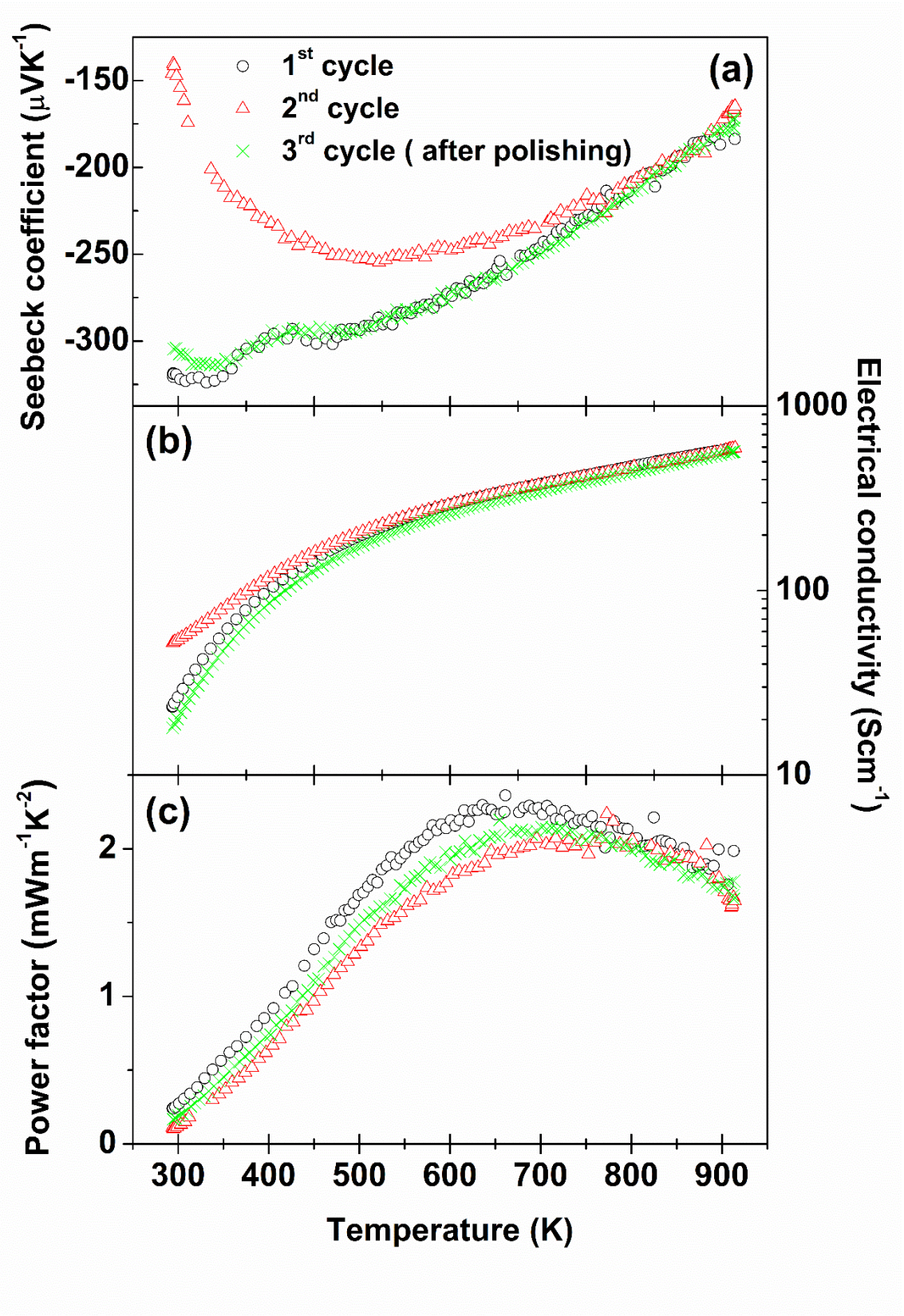
Seebeck coefficient (μVK-1)
-150
-200
-250
-300
1st cycle
2nd cycle
3rd cycle (after polishing)
(a)
(b)
(c)
1000
100
10
Electrical conductivity (Scm-1)
Power factor (mWm-1K-2)
2
1
0
300
400
500
600
700
800
900
Temperature (K)

Supplementary Material

“Role of secondary phases and thermal cycling on thermoelectric properties of TiNiSn half Heusler alloy prepared by different processing routes”

Francesco Aversano[1], Mauro Palumbo[1,*], Alberto Ferrario[2], Stefano Boldrini[2], Carlo Fanciulli[3], Marcello Baricco[1], Alberto Castellero[1,*]

[1]University of Turin, Department of Chemistry & NIS, Turin, Italy

[2]CNR – ICMATE, Padova Unit, Padova, Italy

[3]CNR – ICMATE, Lecco Unit, Lecco, Italy

*Corresponding author:

Mauro Palumbo; Tel. +39 0116707913; Fax: +39 0116707855; e-mail: mauro.palumbo@unito.it

	Elemental composition (at. %)		
Element	Ti	Ni	Sn
Average	33.5	33.0	33.5
Standard deviation	0.5	0.5	0.5

Table 1-S. EDX results for AM-AN sample.

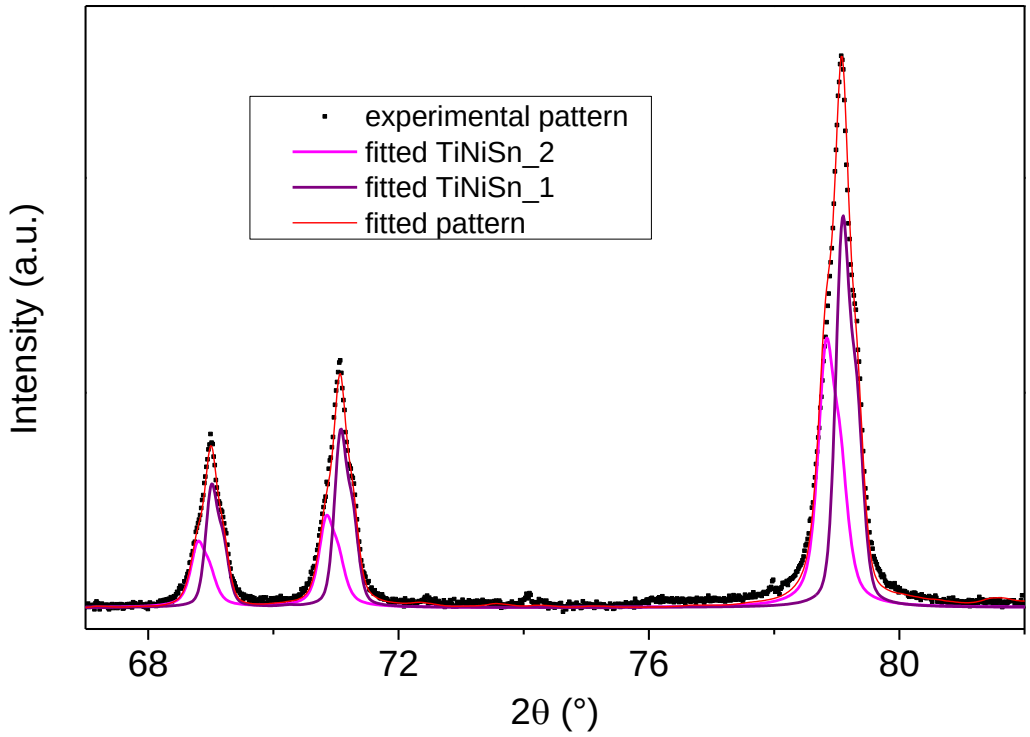

Figure 1-S. Experimental XRD pattern of ODP sample (black dots) and fitted pattern (red line) obtained considering two half-Heusler phases with different lattice parameters (magenta and purple lines) to simulate the inhomogeneous distribution of interstitial Ni in the Wyckoff position 4d in the unary cell.

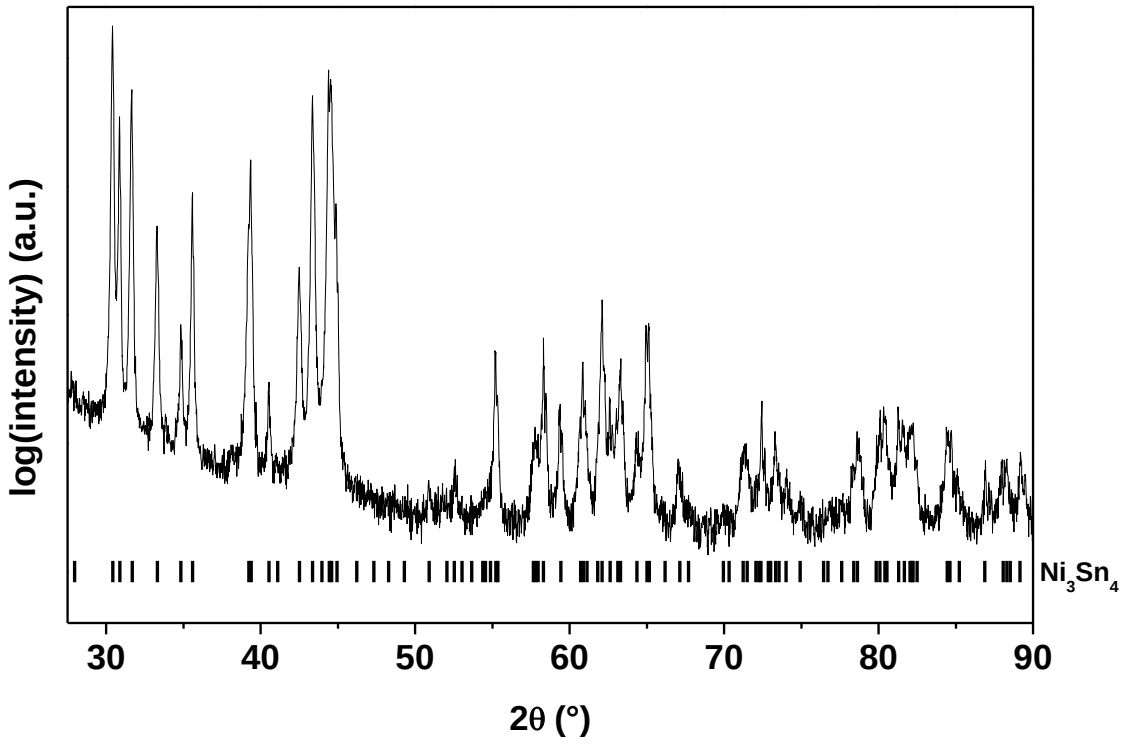

Figure 2-S. XRD pattern of Ni_3Sn_4 alloy prepared by ECAE and subsequently annealed at 873 K for 60 h.

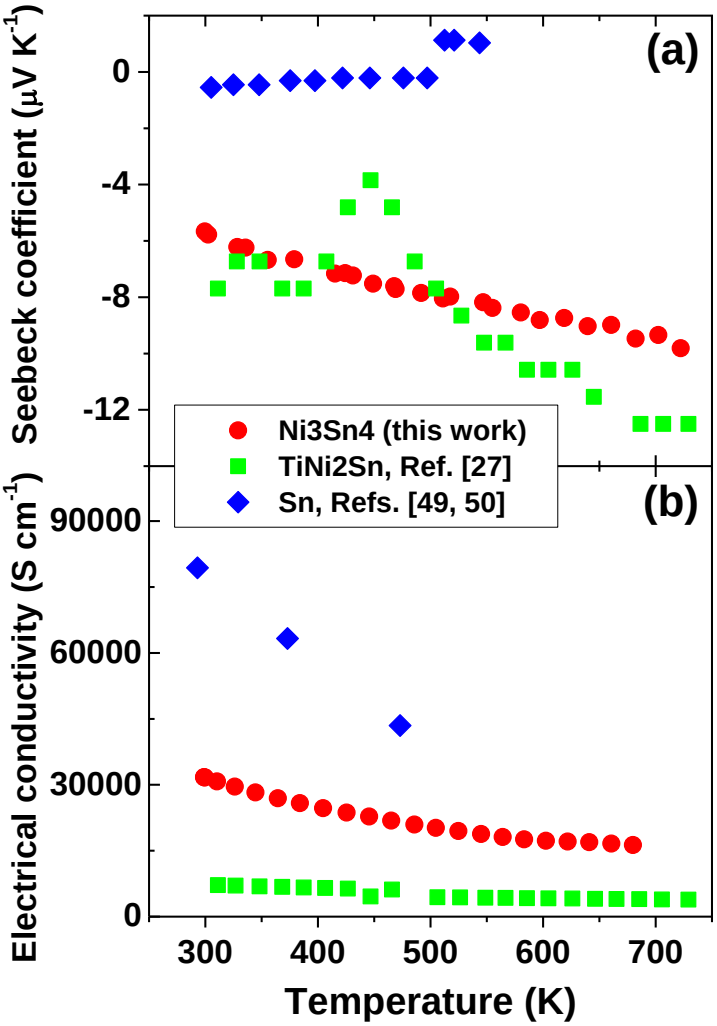

Figure 3-S. Experimental values of the Seebeck coefficient (a) and electrical conductivity (b) as a function of temperature for Ni_3Sn_4 (red circles) [this work], $TiNi_2Sn$ (green squares) [27] and Sn (blue diamond) [49, 50]. References to the literature are the same of the main text.

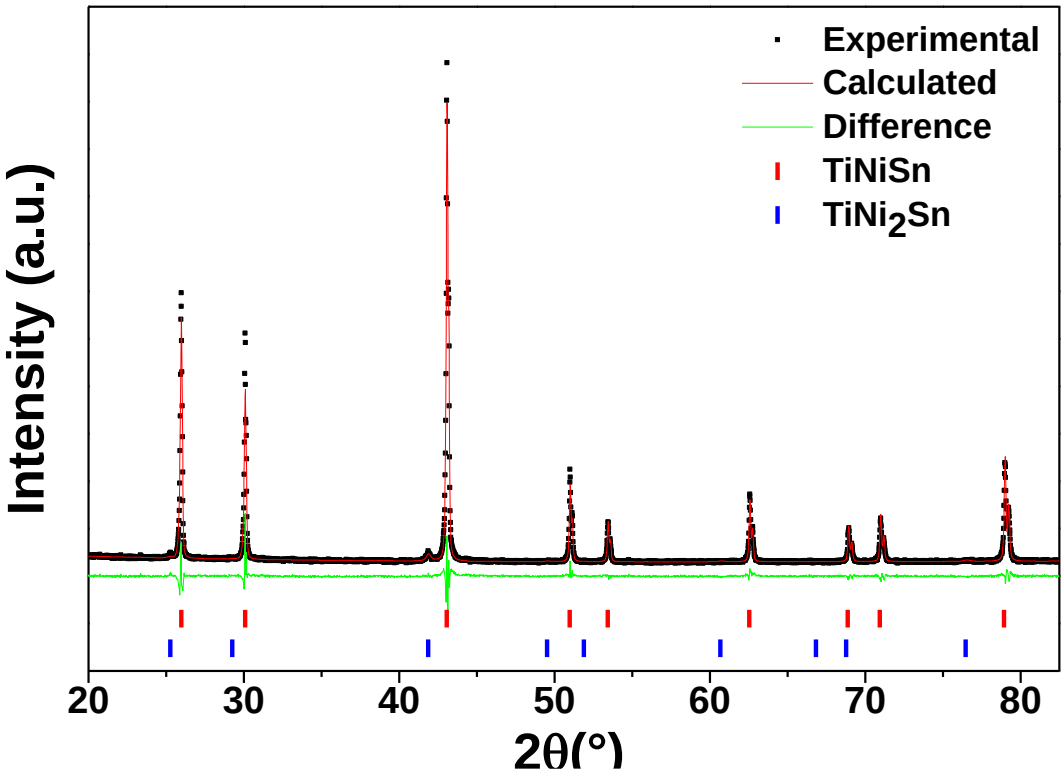

Figure 4-S. XRD pattern of $TiNi_{1.03}Sn$ alloy.

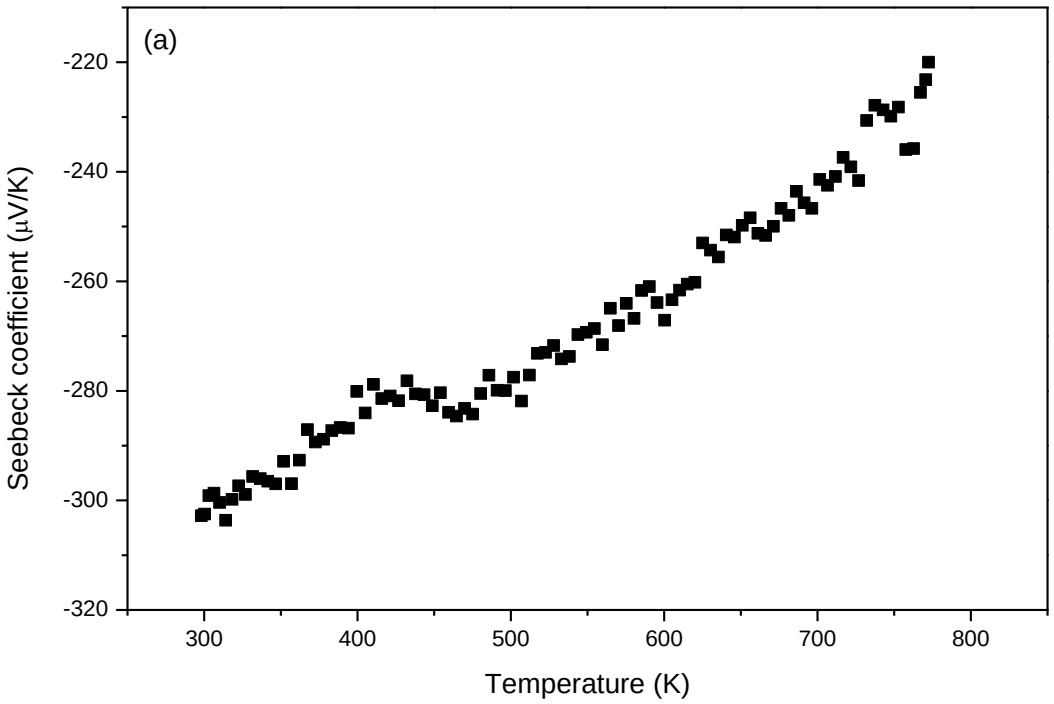

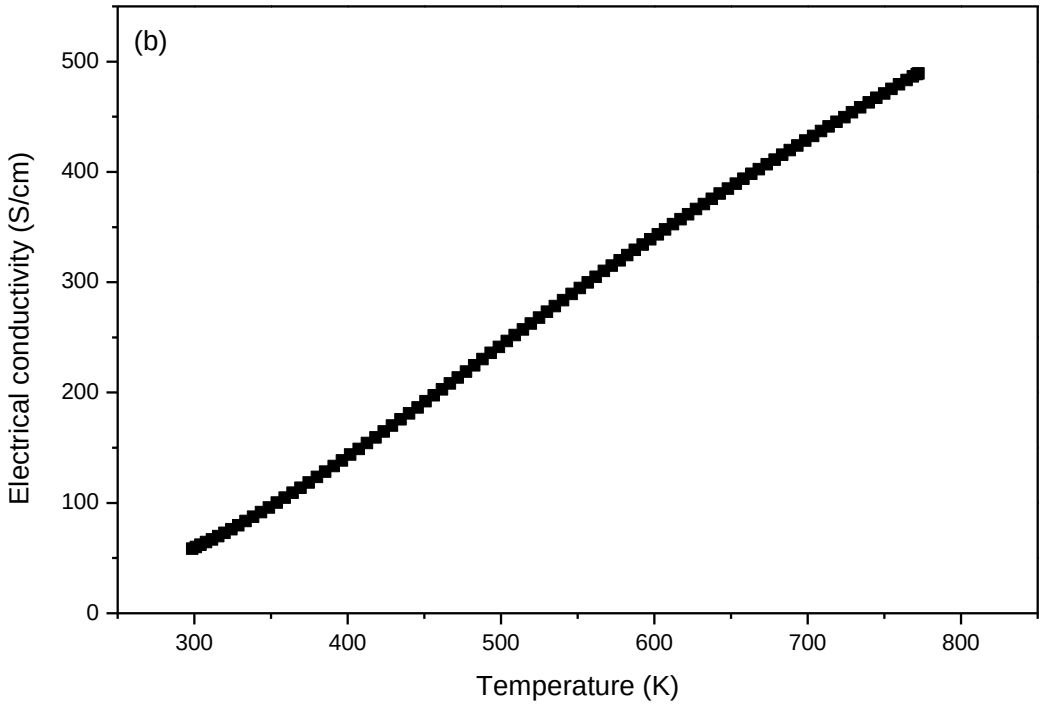

Figure 5-S. Temperature dependence of Seebeck coefficient (a) and electrical conductivity (b) for the $TiNi_{1.03}Sn$ alloy.

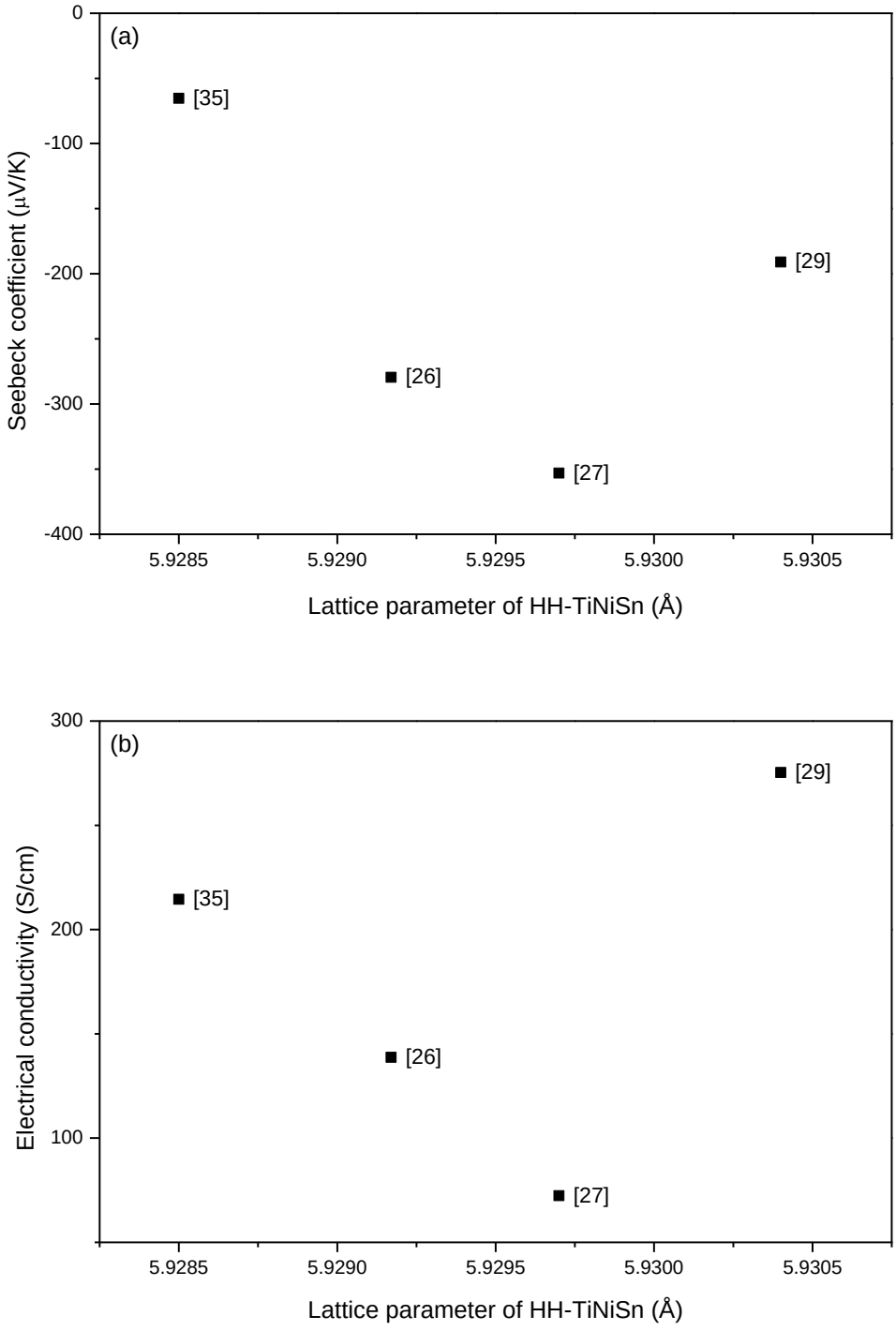

Figure 6-S. Seebeck coefficient (a) and electrical conductivity (b) at 328 K as a function of the lattice parameter of the half-Heusler phase for the samples selected from the literature, as reported in Table 2 and Figure 9 of the main text. References to the literature are the same of the main text.

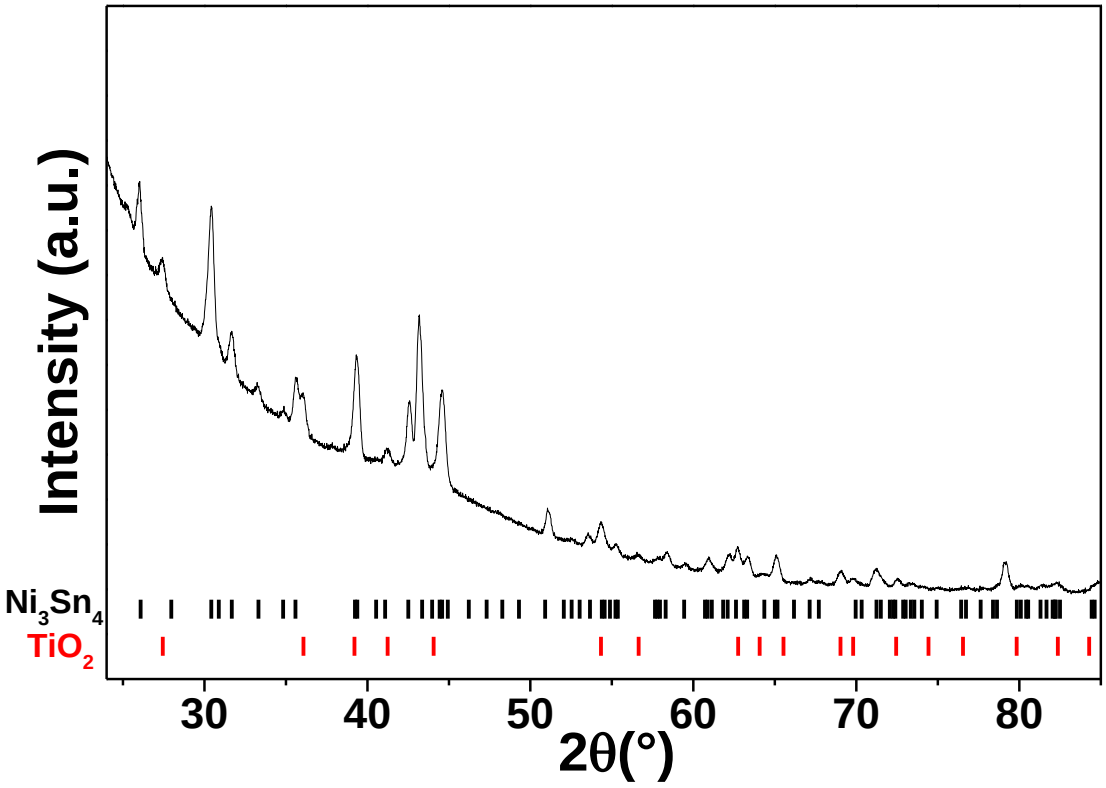

Figure 7-S. Parallel beam X-ray diffraction pattern of the AM-AN sample after the first cycle of the measurement of electrical conductivity and Seebeck coefficient.

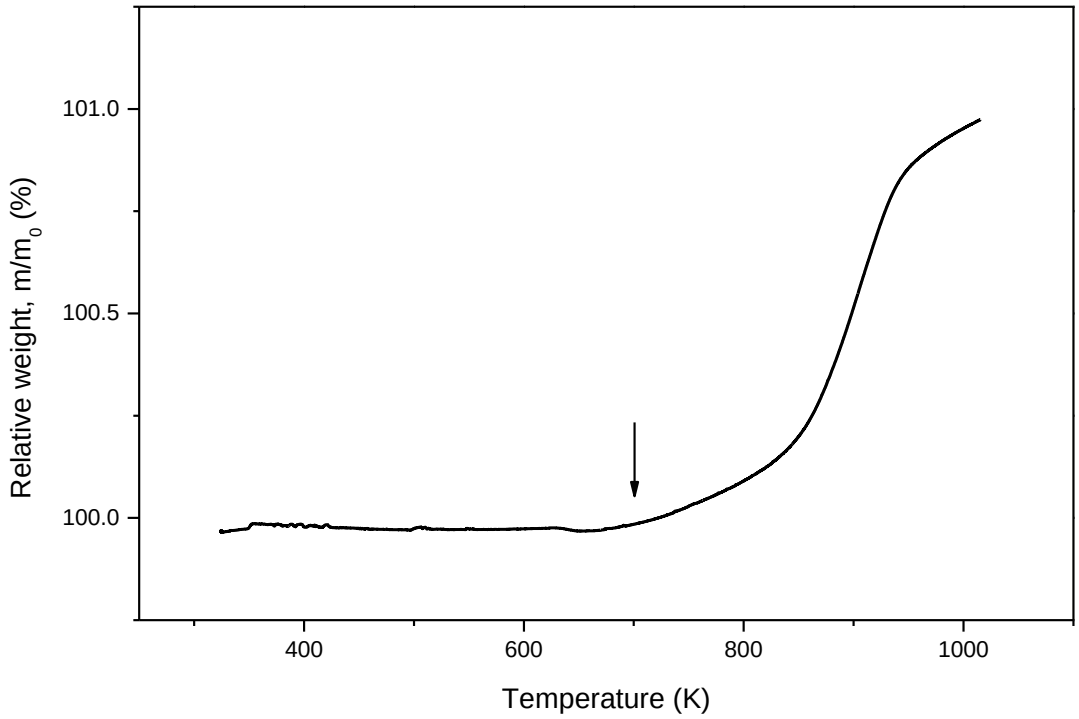

Figure 8-S. TGA trace of the AM-AN sample showing the temperature dependence of the relative weight under N_2 flow.

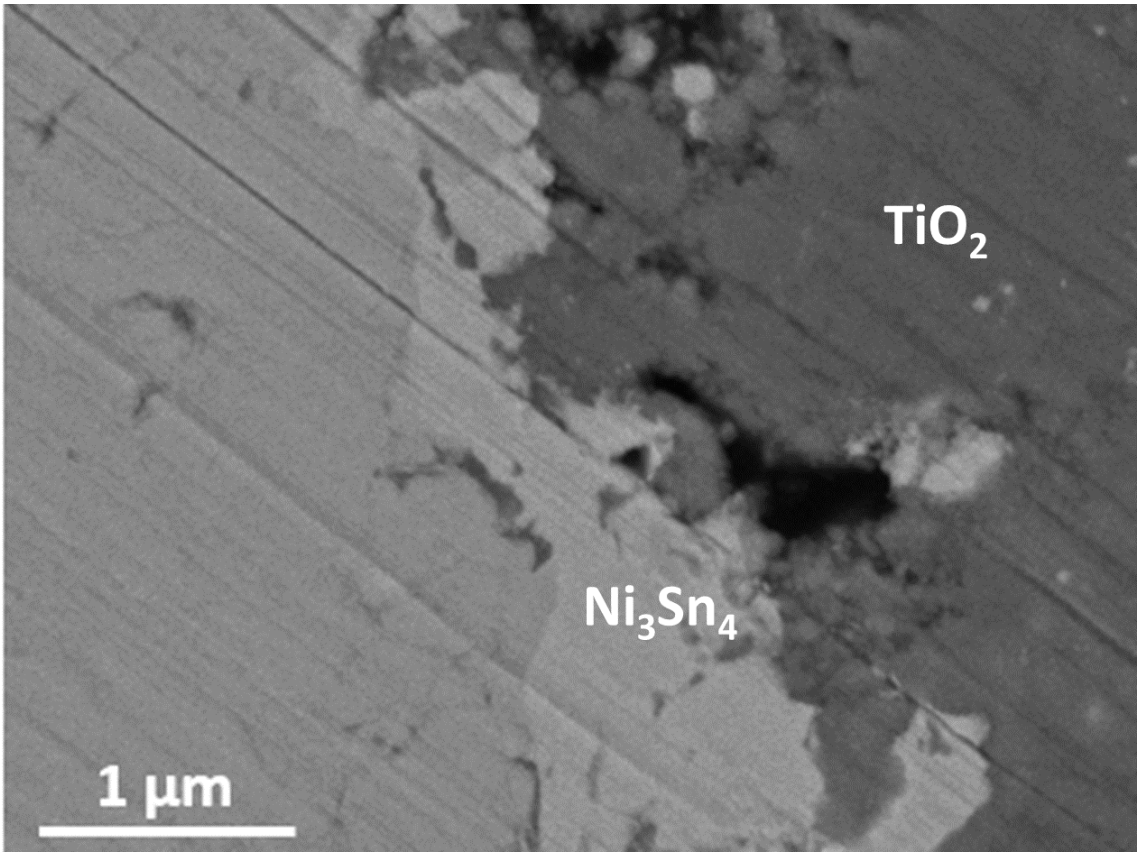

Figure 9-S. Backscattered electrons SEM micrograph of the AM-AN sample after the first cycle of the measurement of electrical conductivity and Seebeck coefficient. The phase contrast shows an altered surface layer containing TiO_2 and Ni_3Sn_4.

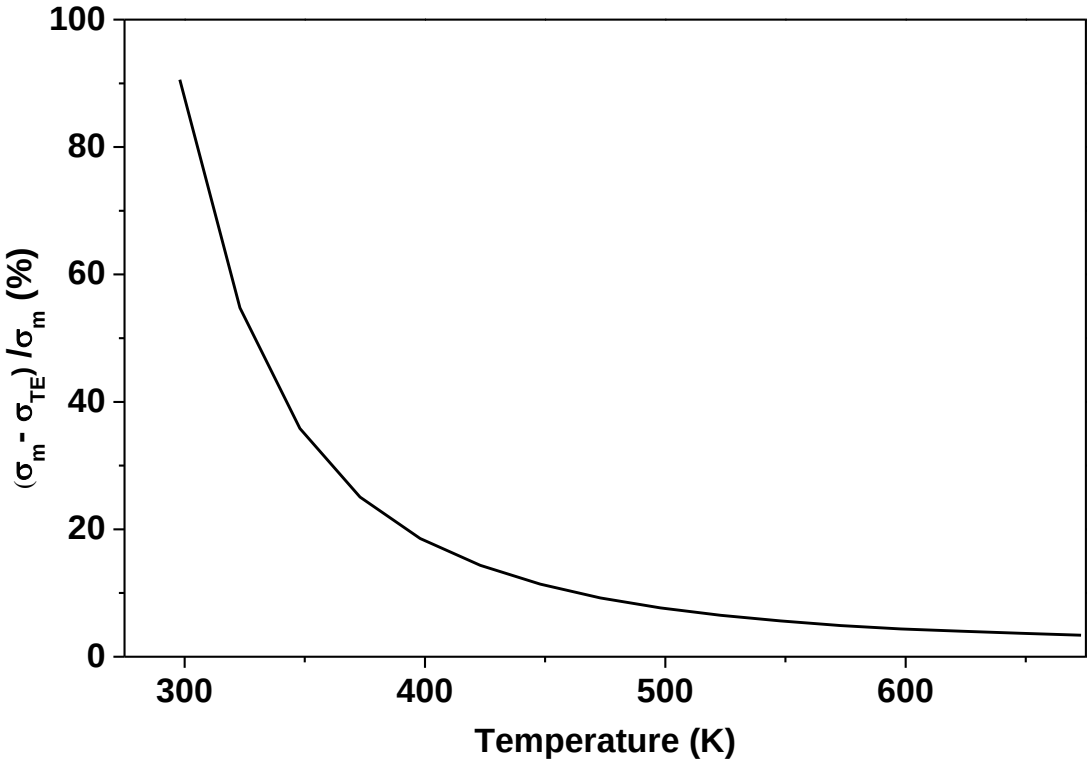

Figure 10-S. Temperature dependence of the relative difference between the electrical conductivity measured in cycle 2 (σ_m) and the electrical conductivity of the thermoelectric material (σ_{TE}), measured in cycle 1.